SERI/STR-211-3083
DE87001159

March 1987

Investigation of Selected Electrically Active Defects in Polycrystalline Silicon Solar Cell Materials

Final Subcontract Report
30 May 1986

J. Hren
University of Florida
Department of Materials Science
and Engineering
Gainesville, Florida

Prepared under Subcontract No. ZB-4-02129-2

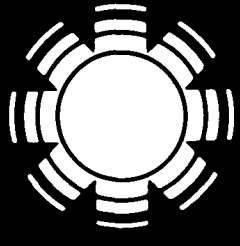

SERI

Solar Energy Research Institute
A Division of Midwest Research Institute

1617 Cole Boulevard
Golden, Colorado 80401-3393

Operated for the
U.S. Department of Energy
under Contract No. DE-AC02-83CH10093

Printed in the United States of America
Available from:
National Technical Information Service
U.S. Department of Commerce
5285 Port Royal Road
Springfield, VA 22161

Price: Microfiche A01
Printed Copy A06

Codes are used for pricing all publications. The code is determined by the number of pages in the publication. Information pertaining to the pricing codes can be found in the current issue of the following publications, which are generally available in most libraries: *Energy Research Abstracts, (ERA); Government Reports Announcements* and Index (*GRA* and I); *Scientific and Technical Abstract Reports (STAR);* and publication. NTIS-PR-360 available from NTIS at the above address.

SERI/STR--211-3083

DE87 001159

SERI/STR-211-3083
UC Category: 63
DE87001159

Investigation of Selected Electrically Active Defects in Polycrystalline Silicon Solar Cell Materials

Final Subcontract Report
30 May 1986

J. Hren
University of Florida
Department of Materials Science
and Engineering
Gainesville, Florida

March 1987

SERI Technical Monitors:
Y. S. Tsuo
J. Benner

Prepared under Subcontract No. ZB-4-02129-2

Solar Energy Research Institute
A Division of Midwest Research Institute

1617 Cole Boulevard
Golden, Colorado 80401-3393

Prepared for the
U.S. Department of Energy
Contract No. DE-AC02-83CH10093

TABLE OF CONTENTS

INVESTIGATION OF ELECTRICAL AND MICROSTRUCTURAL PROPERTIES IN POLYCRYSTALLINE SILICON SOLAR CELL MATERIALS

Manufacturing techniques are being developed to improve the cost effectiveness and energy efficiency of silicon wafers for large scale, terrestrial, solar energy applications. ESP (Edge Supported Pulling) silicon sheets and LASS (Low Angle Silicon Sheets) were the two materials analyzed in this study.

Correlations between the electrical properties and the structural and microstructural properties were investigated in this study. The structural properties were analyzed using the SAEC (Selected Area Electron Channeling) technique while the electrical properties were described qualitatively by means of the EBIC (Electron Beam Induced Current) technique. The Transmission Electron Microscope (TEM) was used to analyze the microstructural properties. No SAEC work was done on the ESP material since the material was received as an already fabricated device and previous research had been done by SERI (Solar Energy Research Institute). Device fabrication on the LASS material was done in-house.

In this investigation it was found that the LASS material was semi-randomly oriented with 81% of the surface normals of the grains

oriented at either [113], [233], [015] or [2 7 16]. In general, the growth direction was parallel to the {211} family of planes. The EBIC results of the ESP material showed long, linear bands of poor electrical response. The EBIC results of the LASS material showed poor electrical response along grain boundaries, and near silicon inclusions and dislocation clusters. The TEM results showed a predominance of twins and stacking faults in the ESP and LASS materials. The LASS material also exhibited grain boundaries, dislocation networks, and precipitates.

This work suggests that the poor electrical response is related to the stacking faults, grain boundaries, and dislocation networks presumably formed by the mechanical pulling during sheet formation. At the same time the dislocation networks often appeared to act as gettering sites to tie up impurities and thereby improve the overall electrical response of the material.

CHAPTER 1
INTRODUCTION

Since the beginning of time man has been fascinated with the sun. The sun has been used to tell time, determine directions and even worshipped as a god. However, the harnessing of the sun as an energy source has previously not been exploited to its fullest. In recent years the limited supply of fossil fuels has become a major concern, making the use of the sun as an energy source for large scale, terrestrial applications a more viable alternative.

Large scale terrestrial applications include the generation of energy for large buildings such as schools, malls, factories, etc. or for separate power substations in remote areas. For these applications solar panels are often placed on the rooftops of large buildings or are set up on land for separate power substations. These solar panels are large rectangular frames approximately 1.65 m x 0.90 m, upon which numerous solar cell devices are mounted in a pattern of parallel and series electrical connections [1-3].

Diverse research has been conducted on improving the manufacturing and performance of solar cell devices for solar panels. Presently, one of the difficulties in improving solar cell devices is determining the best raw material for such devices. Some of the major criteria for raw material selection include: abundant raw material supply, cost effectiveness and energy efficiency. Silicon is one of the materials being considered since it is one of the two most abundant

elements in the earth's crust [4]. Silicon is also fairly easy to work with since it is an elemental semiconductor and does not decompose with processing as compound semiconductors often do [5]. Processing is thus facilitated since partial pressures do not need to be maintained or liquid encapsulation techniques used. Silicon devices can be operated at fairly high temperatures. The upper ambient operating temperature is between 125-175°C [5]. Silicon as a raw material is also quite inexpensive because of its abundance. However, it is relatively impure as mined and the expense and energy of refining does limit its cost effectiveness. Silicon is an indirect band gap material with a band gap of 1.1 eV. This indirect band gap limits the maximum conversion efficiency attainable because of the extra loss in energy output caused by a change in momentum. The maximum conversion efficiency is "the ratio of the maximum electrical power output to the solar power arriving on unit area" [6:778]. Besides the indirect band gap, the maximum conversion efficiency is also limited by the wavelengths of the incoming solar spectrum. Those wavelengths that are longer than 1.2 μm for silicon [7] do not impart sufficient energy for the appropriate carriers to surmount the band gap. Those wavelengths that are 1.2 μm or shorter have sufficient energy to surmount the band gap energy; however, wavelengths which are too short have surplus energy which is lost in inefficient absorption. Thus, the maximum calculated conversion efficiency from silicon solar cells is about 22% [6]. Silicon solar cell devices using present fabrication techniques are reported to have maximum conversion efficiencies which range between 5-19% for an AM1 (air mass 1) rating.

Consequently, for silicon solar cells to be a viable energy alternative it is desirable to fabricate a cell quickly and inexpensively and yet with an energy efficiency approaching 22%. It is this compromise between cost effectiveness and energy effectiveness that has brought about the development of many different fabrication techniques of single crystal, polycrystalline, and amorphous silicon for solar cells. One of the oldest techniques is the single crystal growth of silicon into boules (Czochralski or "Teal-Little" process [1]) and the subsequent sawing and cutting into wafers. Although this material is single crystal and relatively high conversion efficiencies have been achieved (16-19% [8]), approximately 82% of the silicon is wasted manufacturing a cell [1]. To reduce the material waste and thus the cost, new techniques to grow silicon in sheets or ribbons have been devised. These include such techniques as: edge-defined film-fed growth (EFG), ribbon-to-ribbon (RTR), Capillary Action Shaping Technique (CAST), Westinghouse dendritic, etc. Less material loss occurs with these techniques but the grown silicon is polycrystalline and the efficiencies have not been as high as single crystal growth material. Techniques to cast polycrystalline silicon such as Wacker Silso, Heat Exchanger Method (HEM), etc., have also been tried with similar achievements and problems as previously described for ribbon techniques. To reduce the amount of silicon used even more, thin film techniques have been developed. In this technique a thin film of silicon is deposited onto a less expensive substrate by such processes as Chemical Vapor Deposition (CVD), Thermal Expansion Shear Stress (TESS), Low-Pressure-Chemical-

Vapor-Deposition (LPCVD), etc. These techniques are rather complicated and only moderate efficiencies have been achieved with silicon. However, the majority of research on thin films has been done on more exotic materials, so improvements in efficiencies of silicon may be achieved in the future. A new approach is to use amorphous silicon for solar cell devices. The efficiencies of these devices are relatively low when compared with the other techniques; however, the cost of processing is also very low.

In this investigation ribbon growth materials were studied. Many new fabrication techniques are being developed to reduce fabrication costs while maintaining or improving energy efficiencies of these materials. Two new fabrication techniques for silicon solar cells include: Edge Supported Pulling (ESP) and Low Angle Silicon Sheet (LASS).

In the ESP technique the melt is stabilized between two graphite rods which are pulled horizontally through the quartz crucible at a rate of 6-30 mm/min. This technique yields fairly high quality sheets with a maximum conversion efficiency of 13.8% at an AM1 rating [9].

In the LASS technique the melt is stabilized on the bridge of a seed crystal and horizontally pulled out of the melt at a rate of 100-800 mm/min. This technique yields a high throughput of material, although the maximum conversion efficiency is only 12.9% at an AM1 rating [10].

These technological advancements with silicon solar cells are very good; however, to further improve these fabrication techniques

an investigation of the microstructural properties such as grain boundaries, dislocations, twins, etc. and the corresponding electrical effects is required. It is thought that some microstructural perturbations can be electrically active while others are relatively electrically non-active. Electrically non-active defects are those defects which are incapable of controlling the flow of energy, similar to passive circuit components in circuit theory [11]. For example, work by B. Cunningham et al. showed that coherent twin boundaries are generally electrically inactive but that dislocations trapped at these boundaries can be electrically active [12]. Therefore, if these electrically active defects, which disrupt the energy flow, can be eliminated then the energy efficiency of silicon solar cells may be improved.

It was therefore the purpose of this investigation to draw correlations between the electrical response, as qualitatively represented by the Electron Beam Induced Current (EBIC) technique, and certain structural and microstructural defects, as determined by Selected Area Electron Channeling (SAEC) and Transmission Electron Microscopy (TEM), respectively, of ESP and LASS silicon sheet materials.

This report is divided into seven main chapters. Following an introduction in Chapter 1, a review of previous literature on this subject is given in Chapter 2. A brief description is given on how silicon solar cells work, emphasizing those electrical and microstructural parameters which are important in this study. Some of the

work being done on electrical modelling is also reviewed. A detailed description of how ESP and LASS sheets are fabricated is then given. Previous research done by SERI on ESP and LASS materials is reviewed. This is followed by a review of research done on other similar polycrystalline sheet materials. The rationale for the development of the experimental approach used in this investigation is discussed, emphasizing the purpose and limitations of the three main analytical techniques used.

Chapter 3 describes the experimental procedure. Briefly, the general mode of operation and the physical specifics about the samples are introduced. A description of the device fabrication technique used on the LASS material is given. The sample preparations and the setup of equipment for SAEC, EBIC and TEM are then described.

In Chapter 4 the results of SAEC for the LASS material are given. The EBIC results for the ESP and LASS materials are described. Finally, the TEM results for the ESP and LASS materials are given.

In Chapter 5 the SAEC, EBIC and TEM results are interpreted. Correlations between these results are discussed and ideas for improvements in the fabrication techniques are presented. Conclusions from this study are stated in Chapter 6, followed by suggestions for future work in Chapter 7.

CHAPTER 2
LITERATURE SURVEY

Pertinent Electrical Parameters

A basic understanding of how silicon solar cells work is important to correctly interpret the results of this investigation and to elict improvements. Extensive literature has been published on this subject [1,3,8,13-15]. However, from a simplistic point of view a solar cell is a junction, an n-p junction in this investigation, with a depletion region. This inherent charge gradient in the junction sets up an electric field along the junction. Photons of light then hit and penetrate the device. These additional charges create electron-hole pairs and migrate towards the depletion region because of the electric field there. Depending on the energy of the incoming photon, the minority carrier diffusion length, the minority carrier lifetime, etc., the electron-hole pairs may either recombine or may arrive at the depletion region. Those pairs which do arrive at the depletion region are swept through this region and an electric current is generated.

To develop an understanding of the influence of material defects on the electrical properties of solar cell devices, this general description of photoconductivity for an indirect band gap material can be theoretically described by the following equation:

$$\Delta\sigma = q\, g_{op}\, (\tau_n \mu_n + \tau_p \mu_p)$$

where $\Delta\sigma$ = photoconductivity

q = charge

g_{op} = optical generation rate

τ_n, τ_p = recombination lifetime or minority carrier lifetime of electrons, holes

μ_n, μ_p = mobility of electrons, holes

Thus, from this equation it can be seen that high mobilities (μ_n, μ_p) and long recombination lifetimes (τ_n, τ_p) are desirable for high values of photoconductivity. The mobility of a material can be described by the Einstein relation, or

$$\mu = (D \cdot q)/(k \cdot T)$$

where μ = minority carrier mobility

q = charge

k = Boltzman's constant

T = temperature

D = minority carrier diffusion coefficient

If it is assumed that (q/kT) is approximately constant for a set operating temperature then the minority carrier mobility is proportional to the minority carrier diffusion coefficient. However, the diffusion coefficient can be described by the equation:

$$D = L^2/\tau$$

where D = minority carrier diffusion coefficient

L = minority carrier diffusion length

τ = minority carrier lifetime

Thus, from these equations, the photoconductivity is proportional to the square of the minority carrier diffusion length (MCDL) which is "the average distance a free charge carrier can diffuse in one lifetime period in a semi-infinite material" [16:11].

The mobility, minority carrier lifetime, and minority carrier diffusion length are all material related properties which are inversely proportional to the probability of recombination occurring. Therefore, discontinuities in the crystal network such as from grain boundaries, dislocations, etc. could provide sites for electron-hole pairs to recombine and thus increase the probability of recombination, which would decrease the photoconductivity.

Three basic models have been proposed concerning the electrical effects at grain boundaries. One model is the segregation model where it is assumed that impurity atoms segregate to grain boundaries where they become electrically inactive [17]. Research has shown that the amount of phosphorous segregation does vary from grain boundary to grain boundary [18]. However, this model does not correctly predict the observed temperature dependence [16]. A second model is the double-depletion-layer thermal emission model which shows that the barrier height is temperature dependent and that the changing of the interface state by the diffusion of atomic hydrogen down grain

boundaries is important [16]. This model has formed the basis for alkali passivation research. The third model is the grain boundary trapping model and "is based on the existence of a large concentration of active trapping sites at the grain boundary which serve to capture free carriers" [16:8].

Material parameters which influence the grain boundary trapping model, i.e., the nature of this grain boundary, include the grain boundary: size, width, effective width, trap density, and trap energy. In the grain boundary model, as in many of the models, grain boundaries are assumed to be flat planes. This assumption gives insights as to what is happening but leads to difficulties in rigidly applying these models to real materials. The grain size (d_{gb}) is the average distance between grain boundaries [16]. The grain boundary width (l) is the "actual width of the region of crystallographic change from one grain to another" [16:10]. However, the area of influence of the electrical effects around a grain boundary are much wider than the grain boundary width and so the effective grain boundary width (l_{eff}) can be described as "the width at which the conduction and valence bands return to their mid-grain values" [16:10]. The trap density Q_t (cm^{-2}) is the number of grain boundary traps N_t (ev/cm^2) and is "measured with respect to the intrinsic Fermi level energy" [17:5250].

The surface recombination velocity (s) is the rate of recombination at a surface and is assumed to be proportional to the product of trap density per unit area, capture cross section per trap, and the thermal velocity [16]. The grain boundary effective surface recombination

velocity (S_{eff}^{gb}) is analogous to the surface recombination velocity except the surface is a grain boundary.

As previously described, photoconductivity is proportional to the minority carrier diffusion length. However, the minority carrier diffusion length is proportional to the recombination lifetime and the surface recombination velocity. Thus it is the minority carrier diffusion length, the surface recombination velocity, and the recombination lifetime which determines the short circuit current response. It is this current response which is qualitatively described in the EBIC technique in this investigation [16,19].

Traps such as grain boundaries, dislocations, etc. which affect the minority carrier diffusion length, surface recombination lifetime, and recombination lifetime also affect the electrical properties of a solar cell device. Thus an understanding of how the ESP and LASS materials are fabricated is beneficial in determining what types of defects can be formed and how they can be eliminated.

Fabrication Techniques

The ESP technique was developed around 1980 by T. F. Ciszek and J. L. Hurd of the Solar Energy Research Institute (SERI) [9]. In general, a semiconductor grade melt is doped with boron to form 1 Ω-cm resistivity sheets and surrounded by a one atmosphere argon environment. Two 1.5 mm diameter dense graphite rods are connected to a silicon or graphite bridge about 40 mm wide. Dense graphite or graphite multifiber

filaments were used because of the closeness in the thermal expansion coefficients with the silicon sheets. This assembly is immersed into the melt through two holes in the bottom of a quartz crucible in an R.F. induction-heated graphite susceptor. The two holes in the crucible are slightly bulged down to help prevent leaking. The melt is also maintained at about one half of the maximum stable height (h) to help prevent leaking. The maximum stable melt height is approximately equal to 67.4 divided by the hole diameter (ϕ) - 5.82 [9]. After the bottom of the bridge has made contact with the melt, the assembly is mechanically pulled up at a rate of 0-30 mm/min as crystal growth proceeds. The bridge assembly can be seeded or nonseeded for this technique. See Figure 1 for a schematic of this process [20].

The LASS technique is a spinoff from the Horizontal Ribbon Growth (HRG) work by Bliel in 1969 on germanium and ice crystals [21]. Improvements on this HRG process for silicon were reported by Koyanagi and Kudo in the mid-1970s [22-23]. Finally in 1979, the LASS technique was developed by D. N. Jewett and H. E. Bates of Energy Materials Corporation (EMC) [24-25].

Solar grade silicon doped with boron to form sheets with resistivities in the range of 0.5 to 4 Ω-cm is melted in a shallow rectangular quartz crucible in an argon atmosphere. The quartz crucible is located on carbon plates on top of five insulated, resistance heated, hot zones in a water cooled, aluminum furnace. The fifth zone is used to melt solid chunks of material for replenishing the liquid silicon in the other four zones [26]. A seed crystal is mechanically lowered

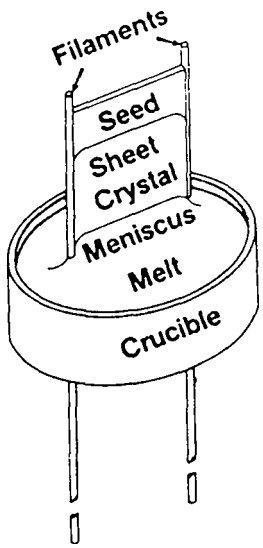

Figure 1. Schematic of the ESP process showing the two graphite filaments being pulled up through the crucible and melt [20:614].

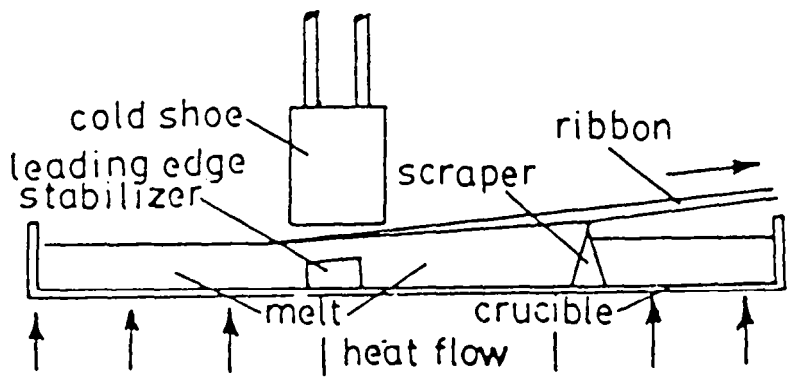

Figure 2. Cross sectional schematic of the LASS process [25:86].

into the melt. The cold shoe is then lowered into place and the flow of cooling gas (He) through the shoe is increased. The effect of the cold shoe and the leading edge stabilizer promote initial crystal growth. The seed crystal is then slowly pulled horizontally or at a small positive angle out of the crucible and over the scraper. The scraper serves as a point of detachment of the ribbon from the melt surface [25]. After the initial crystal growth has stabilized the ribbon can be pulled at a rate of 100-800 mm/min. See Figure 2 for a cross sectional schematic of the growth zone [25].

Three types of grain structure have been identified in LASS samples: random dendritic, parallel dendritic, and twin-stabilized planar growth. Random dendritic material is composed of more or less random intersecting dendrites that have grown within ± 30° to 40° of the gross ribbon growth direction [26]. The top surface roughness of random dendritic material is on the order of 0.2 to 0.5 mm, with large primary dendrites and finer secondaries that fill the interstices [27]. The bottom surface of random dendritic material is somewhat irregular for thinner ribbon (0.4 to 0.5 mm), while for thicker material (0.5 to 1 mm) it is quite smooth [27]. Parallel dendritic material is composed of a regular array of dendrites parallel to the growth direction with the peak-to-peak spacing of the dendrites varying less than 1 to 3 mm [27]. The third type of grain structure, twin-stabilized planar growth, is characterized by a smoother top surface with parallel, faceted surface structures less than 0.1 mm high and with peak-to-peak spacings of about 0.5 to 0.8 mm [27].

Previous Research

At present, the majority of research work on the correlation of electrical and microstructural characteristics of ESP and LASS materials has been done by the Solar Energy Research Institute (SERI).

Edge Supported Pulling

Most of the research done by SERI on ESP materials has been on silicon sheets doped with boron to form a 1 Ω-cm resistivity [20]. On these samples neither a phosphorous layer to form an n-p junction nor an oxide coating were deposited; however, on later research these materials were used. The sheets were then cleaned and polished. A 500 Å layer of either titanium or aluminum was vacuum evaporated onto the front to form the Schottky contact and a layer of gold was vacuum evaporated on the back to form the ohmic contact. The EBIC and SAEC analyses were then done on the sample. Three thicknesses of samples were evaluated: 110 μm thick material formed at a pull speed of 30 mm/min, 480 μm thick material formed at a pull speed of 12 mm/min, and 1100 μm thick material formed at a pull speed of 8 mm/min. Generally for the SAEC technique, only grain widths larger than 0.5 mm were evaluated and all small grains located 3 mm or less from the graphite filaments were ignored.

It was observed using the Scanning Electron Microscope (SEM) that the ESP sheets were composed of long, linear grains in the center and short, spurious grains on the edges near the filaments. It was felt that the short, spurious grains along the edges helped to control the

further nucleation and growth of crystals so that long, linear grains could develop in the bulk of the material.

The results of the electron channeling study varied with the thickness of the samples. The electron channeling results for the 1100 μm thick material showed that both the surface normals and the direction of grain growth were randomly oriented. On the other hand, the 480 μm thick material had three quarters of the surface normals oriented less than about 16° off of the [011] direction. The plane parallel to the growth direction for these latter grains was close to the $(11\bar{1})$ plane. The surface normals of even thinner, 110 μm thick material were all oriented less than 20° off of the [011] direction and three quarters of the growth directions were closely parallel to the $(11\bar{1})$ plane. Thus the tendency of the thinner, slower pulled material was to become more oriented like single crystal material.

The results of the EBIC study also varied with the thickness of the samples. The EBIC measurements showed that for the 480 μm thick material long, linear bands of EBIC response were observed and that there were sharp differences in intensity of the EBIC signal from grain to grain. The correlation of the EBIC with the electron channeling study showed that the light bands of EBIC response or material of good electrical quality had grains with surface normals oriented near the [011] direction. The light bands of EBIC response were those with dislocation densities less than 5×10^3 cm^{-2} (as determined by counting recombination centers in 100X magnification EBIC pictures). The dark bands had dislocation densities of 2×10^5 cm^{-2} or more. The samples were Secco etched to enhance the topography.

A comparison of SEM topographical photographs and the electrical activity, as deduced from EBIC photographs, gave several correlations. Slight discrepancies were attributed to electrically inactive boundaries, i.e., first order coherent twins. The 110 μm and 1100 μm thick samples showed very little variation in intensity of EBIC response from grain to grain. However, the overall EBIC signal was significantly higher for the 110 μm thick material than for the 1100 μm thick material.

Very large grains can be grown when a seed crystal of the dominant grain structure orientation, e.g., the (011) orientation, is used. This dominant grain orientation is similar to that of edge-defined film-fed growth material. It is probable that the $(11\bar{1})$ twin planes can block the short, spurious growth, which occurs near the filaments, so that the long, linear grains characteristic of the center portion can proliferate. Thinner samples are more conducive to this growth pattern and they should have lower dislocation densities because dislocation climb and geometrical outgrowth are more likely.

From the above results, it was concluded that better electrical response in ESP materials comes from a dominant grain structure composed of long, linear grains with surface normals oriented close to the [011] direction and with growth directions nearly parallel to the $(11\bar{1})$ plane.

Low Angle Silicon Sheet

The research work done by SERI [27] on LASS was done on silicon sheets doped with boron to form a 4 Ω-cm resistivity. There were two sets of samples investigated in this study. One set of samples was

composed of twin-stabilized planar growth material while the other set of samples contained a combination of twin stabilized planar growth in the center portion and random dendritic on the edges. The samples were mechanically lapped, chemically-mechanically polished, etched with a Secco etch and then electron channeling was done. The samples were again chemically-mechanically polished and fabricated into devices by either diffusing an n-p junction or by forming a Schottky barrier type diode. The EBIC studies and measurements of the solar cell efficiency, spectral response, and minority carrier diffusion length were then done.

The results from the electron channeling study showed that the twin-stabilized planar material was essentially single crystal with surface normals oriented in the [111] direction. The surface topography of the twin-stabilized planar material was characterized by parallel, faceted structures which tend to run along the [211] direction. It has also been observed that sometimes under the parallel, faceted structures there were clusters of dislocations, usually located under the peaks while the stacking faults were usually located under the valleys. High dislocation cluster densities were generally observed in areas where the twin stabilized planar material was approaching random dendritic material. From the correlation of EBIC and SEI, these clusters were found to be electrically and topographically similar. The stacking fault planes tended to intersect the (111) sample surface along the three <011> directions.

From the EBIC, polycrystalline silicon inclusions, dislocation clusters and large dislocation loops were also observed. The inclusions

were about 0.4 mm^2 in size. The crystallographic orientations of the dislocation clusters were different than that of the surroundings. It was noticed that the dislocation clusters tended to go through the entire thickness and that they tended to grow larger toward the bottom surface than the top. The large dislocation loops were less than 100 μm in diameter, had a density of less than about 3 cm^{-2} and tended to have the same crystallographic orientation as their surroundings.

Eleven cells 0.1 cm^2 in area and two cells 1.6 cm^2 in area were fabricated into devices with a diffused phosphorous layer, back surface field (BSF) formation and an antireflection (AR) coating. The AM1 efficiencies for the larger solar cells were 10.9% and 11.3%, for the smaller solar cells from 8.9% to 12.7%, and for the two control cells (2.5 Ω-cm Czochralski grown, 1.6 cm^2 in area) were 14.8% and the larger, 10.9% efficient cell was 16 μm and from a control cell was 164 μm. The spectral response of the 10.9% efficient, larger solar cell was compared to a control cell. The response of both was similar for wavelengths shorter than 0.60 μm, but at 0.70 μm the LASS peaked and dropped off rapidly while the control cell dropped of at 0.90 μm.

It was hypothesized that there were pools of liquid regions behind the growth front which were trapped by thin layers of the solid regions. When these pools finally froze, the silicon would expand, creating the surface topography and defects such as dislocations and stacking faults observed in the LASS material. They observed that the defects were larger on the bottom than on the top. They felt that this correlated well with the hypothesis about Czochralski growth in

which the ribbon continues to grow even after the growth front has moved on.

EMC has also done some preliminary research on LASS materials. They were working with 1 Ω-cm boron doped material fabricated into devices similar to SERI. They observed that the random dendritic material is polycrystalline with the presence of twins and a few high angle grain boundaries [26]. The parallel dendritic material has surface normals typically 20 to 30° off of the <110> direction with growth directions at either <210> or <211>. They also remarked that "the growth of dendritic ribbon at times displays a susceptibility to uncontrolled thermal variations which has been attributed to convective instabilities in the melt" [26:304]. These disturbances in the melt can be easily transmitted to the leading edge and seen as a change in the effective pull angle [26].

Spark source mass spectrometric analysis done on some of the ribbons showed levels of Fe, Cr and Al contamination. This contamination of the melt was also given as the main reason for the low end values of the minority carrier diffusion length as measured by surface photovoltage measurements which were in the range of less than 10 μm to 85 μm [25].

Other device measurements included a fill factor of 0.75, open current voltage of 0.536 V, short circuit current density of 32.1 mA/cm^2 and efficiency of 12.9% [24].

Passivation

Besides improving the fabrication techniques, another method for improving the electrical qualities of these materials presently being researched is that of hydrogen or alkali passivation.

The premise behind passivation is that "at a typical silicon grain boundary, it is the presence of atoms which are not tetrahedrally coordinated (the so-called "dangling bonds") which are thought to give rise to the most effective recombination sites" [28:337]. Thus, introduction of hydrogen or alkali atoms into the area of the defect ties up or passivates these "dangling bonds" and reduces barrier heights, electrical resistance, and recombination. This process has been tried on a variety of materials and experimental setups [28-36]. Some of the first research was done by C. H. Seager and D. S. Ginley at Sandia National Research Laboratories [28]. The R.F. glow discharge process was used to create the plasmas. Besides hydrogen, plasmas of O_2, SF_6 and N_2 were also employed at 400°C and 10^{-1} Torr. Two observations were made. Firstly, the maximum temperature (400°C to 425°C) and the duration of the process were not energy intensive. Secondly, the hydrogenated samples were stable since there was no decay of the barrier conductance even after annealing at 320°C for more than 50 hours. It was also indicated that passivation with monatomic hydrogen results in increases in conductance but decreases in the initial free energy (G_o). Passivation in hydrogen does not seem to reduce the grain boundary state concentration. The absorption of oxygen as well as the desorption of hydrogen may occur in boundaries during vacuum

anneals. The boundary conductance seems to be able to be cycled between high and low values an unlimited number of times. Finally, after such limited experimental work the mechanism could not be determined but two theories exist: either the hydrogen simply ties up unsatisfied bonds of nontetrahedrally coordinated silicon atoms or it performs significant reduction of any Si-O bonds which might be present at a grain boundary.

Further work was done by P. H. Robinson and R. V. D'Aiello using a similar experimental setup but emphasizing direct solar cell parameters [29]. They found that with passivation all of the test cells increased in efficiency, the cells with the lowest initial efficiency showed the largest increase after hydrogenation, that both the cell fill factor and the open circuit voltage showed a large increase, and the short circuit current showed little or no variation.

Research was then pursued to directly implant hydrogen since the passivation of small grained polycrystalline silicon by the R.F. glow discharge process to remove only about 80% of all grain boundary recombination losses would be too time consuming [30]. Much of this work was done at Sandia National Research Laboratories by J.K.G. Panitz et al. using a Kaufman ion source on both single crystal and polycrystalline silicon and also on edge-defined film-fed growth (EFG) solar cell devices [31]. Passivation experiments were done using maximum hydrogen ion energies of 900, 1600 and 2300 eV; various energy spreads of ions in the beam; ion current densities of 0.8, 1.4 and 2.0 mA/cm^2; total dosages of 1×10^{18}, 2×10^{18} and 4×10^{18} ions/cm

and bulk sample temperatures during bombardment of 200°, 275° and 300°C. Direct solar parameters were measured. Their results indicated that there was a change in the properties of hydrogen-ion-bombarded silicon with both the maximum ion energy and the ion current density (or dosage rate) and also with a significant parametric interaction between the current density and the bulk sample temperature [31]. Panitz et al. found that for the conditions studied, changes associated with hydrogen ion bombardment were independent of the dose [31]. There also was a noticeable increase in the cell efficiency of EFG devices under optimum conditions.

Research was done by J. I. Hanoka et al. on EFG devices. They found that there were significant improvements in solar cell efficiency for both low diffusion length starting material (about 20 μm) and high diffusion length starting material (about 50 μm) [32].

The EBIC technique was used to investigate the extent of hydrogen passivation and diffusion along grain boundaries of EFG devices. It was stated that two processes may affect passivation. One was the actual diffusion of the hydrogen, estimated to be about 10^{-8}-10^{-9} cm^2/s down the grain boundary. The other was the actual passivation due to the diffusing hydrogen [33]. Also it was shown that increasing values of S (surface recombination velocity) gave lower passivation depths and that for $S > 2 \times 10^4$ cm/s there is a spatial proportionality between the recombination centers (ln S) and a finite distance from the sample

edge to the beginning of significant recombination along the grain boundary [33].

Passivation experiments were also done on dendritic web and ESP solar cells [34-35]. The ESP material was used to study the diminishing passivation effect after repeated EBIC scans. It was proposed that there was electron-beam-induced breaking of the passivated bonds but that annealing at 200°C tended to restore the original passivated condition [36].

Preliminary investigations have been carried out at the University of Florida using a Colutron ion source [37]. The Colutron ion source is a much more narrow, low current density, high energy beam as compared to the Kaufman source.

Therefore, to further improve the energy efficiency of silicon solar cells, whether by fabrication techniques or passivation, a thorough characterization of microstructural perturbations and respective electrical properties needs to be done. This type of research can be done in a variety of ways and work on other similar materials can often provide guidance in experimental procedures and interpretation of results.

Related Research

In general, the various silicon sheet growth methods can be described by three classifications of meniscus geometry [21]. The first classification is M1 which is typified by "close physical proximity between the melt shaping device (or feed stock ribbon, in the case of

RTR) and the solid/liquid interface of the growing ribbon" [21:318]. The close physical proximity does create potential problems with thermal, mechanical and purity control. Typical techniques which fall in this classification are Stepanov, EFG, RTR, CAST and Inverted Stepanov. The second classification is the M2 meniscus geometry classification. The ESP technique falls into this category. Ribbons made from techniques in this classification typically rise from a broad melt base to the sheet interface at a height on the order of 6 mm to 7 mm [21]. These materials have a "greater tolerance to mechanical and thermal perturbations, since no melt shaper is close to the solid/liquid interface" [21:320]. Other fabrication techniques in the M2 classification include WEB, RAD, SOC, CCC, etc. The third classification is M3 and the LASS technique falls in this meniscus geometry classification. Ribbons made from techniques in this classification generally have a very large solid/liquid interface compared to the cross sectional area. The M3 technique tends to achieve very high growth rates because of the high solid to liquid interface area and the corresponding ability to efficiently extract the latent heat of fusion [21]. Other fabrication techniques in the M3 classification include HRG, SCIM version of SOC, RQ and ICC [21].

A great deal of research has been conducted on materials in the M1 meniscus geometry classification. Two materials which fall in this classification are Edge-Defined Film-Fed Growth (EFG) and Ribbon-to-Ribbon (RTR). In the EFG technique, a ceramic shaping guide with a seed crystal of silicon makes contact with the molten silicon and is vertically pulled as growth proceeds [38].

The equilibrium defect structure of EFG ribbon mainly consists of <110> surface normals, <112> growth directions and linear twin bundles which lie parallel to the <112> growth direction [40]. This material has relatively high dislocation densities of 10^4-10^6 cm^{-2} and twin densities of 10^2-10^4 per cm [39]. There are many of the coherent twins on [111] planes which intersect the (110) surface of the ribbon along <112> traces.

The EBIC contrast of this equilibrium defect structure shows a variety of electrical responses from inactive to fully active twins. The dotted EBIC contrast often see in irregular spots is characteristic of partially active twins. Cunningham et al. conducted research on the correlation between EBIC and etching studies [40]. It usually has been assumed that all "linear boundaries, or bundles of linear boundaries, with 111 <112> traces are first order coherent twin boundaries" [40:238].

Research using high voltage transmission electron microscopy (HVTEM) with EBIC has shown that the partially active dotted EBIC contrast along first order coherent twins could be from one of two mechanisms: the presence of partial dislocations in the boundary or the formation of a second order twin joining the first order coherent twins oriented along different {111} planes [40]. The common boundary between the twins could be an incoherent first order {112}/{112} twin boundary or a second order coherent {111}/{115} twin boundary. The {112}/{112} boundary tends to grow out at the surface or to react with first order coherent {111} twins. However, the {111}/{115} boundary is composed of "a large fraction of dangling bonds since 'combs' of single

and double bonds oppose each other" [40:238]. It was suggested that the dotted EBIC contrast was the result of strong minority carrier recombination at the {111}/{115} sections of the boundaries and the absence of recombination along the coherent first order sections [40]. It was also pointed out that the {111}/{115} boundaries could also act as gettering sites for carbon and other impurities. The presence of {111}/{115} boundaries might also explain the inconsistencies between the EBIC results and the etching studies, since the electrical properties would be interrupted but the common {111} plane would etch similarly.

Impurities, precipitates and dislocations were also observed in EFG material. Impurities such as carbon, aluminum, iron and other transition elements were thought to have come from the dissolution of the fused silica crucible, unpurified graphite components or by accident [39]. The effect of impurities on solar devices was influenced by the shape of the interface and the speed of growth. Small precipitates approximately 10 nm in size were found to form frequently at the dislocation nodes of process induced networks while larger precipitates approximately 1 μm in size were most likely formed in the melt [41]. These precipitates were always observed surrounded by dislocation networks which aided in gettering [41].

Besides dislocation networks around precipitates, dislocation helices in the diffused phosphorous region were also observed. The multiplication of dislocations and glide also led to the creation of low angle boundaries which reduce the strain field of a configuration

of dislocations [41]. This multiplication of dislocations and subsequent creation of low angle boundaries was attributed to the relatively long processing time as compared to the short cooling time at temperatures below about 700°C where dislocation motion can easily occur [41].

The RTR material has similar {110} growth surfaces and twin boundaries lying on {111} planes, as observed in the EFG material. Dislocations in twins of RTR ribbons also generated dotted EBIC contrast as seen with EFG ribbons. A typical dislocation arrangement in RTR material is two closely spaced dislocations connected between two parallel twin boundaries spaced about 2 μm apart [12]. A determination of the nature of this dislocation arrangement was not made because the faults overlapped [12].

The silicon-on-ceramic (SOC) technique falls in the same M2 meniscus classification as the ESP technique. In this technique a thin, continuous coating of silicon is placed on a ceramic substrate. This technique also gives the "equilibrium crystalline structure in which the surface of the ribbon is close to {110}, the growth direction is [211], and significant numbers of twin planes lie parallel to the growth direction and perpendicular to the surface" [42:59]. Dotted EBIC contrast has also been noted for SOC as for EFG and RTR. It was felt that the dotted EBIC contrast noted in these three materials was either due to individual dislocations lying steeply inclined in the boundary or from small sections of incoherent twin boundaries which shared a common habit plane with coherent first order twin boundaries [12].

The dendritic-web (Web) technique is similar to the ESP in meniscus classification; however, the dendritic grain structure and preferred orientations are more similar to the LASS material. This technique is a vertical growth technique in which a thin ribbon of single crystal silicon is shaped during growth by crystallographic forces and surface tension, rather than by graphite rods or dies [43]. Maximum conversion efficiencies of 15.5% have been achieved with this material. Deep level transient spectroscopy (DLTS) was used to measure bulk lifetime which ranged from a high of about 30 μsec to a low of less than 3 μsec [44]. The low bulk lifetime was associated with molybdenum contamination from components in the growth system. Crystallographically, the web surface is parallel to the (111) plane, and the web pulling direction is along the <112> direction [45]. The presence of twins, dislocations and stacking faults have also been observed in this material. In general the material between the dendrites if of very high quality.

The most prominent structural feature in Web material is the presence of multiple twin lamellae in the center of the ribbon covered by two thick surface layers which are also in twin relation [45]. In most Web materials, bundles of very long dislocations parallel to <112> are piled up against these 'win planes which are located in the center of the ribbon and parallel to the surface. It is probable that the defect layer between the two, perfect, twin lamellae act as a gettering center for dislocations. Measurements of bulk dislocation densities ranged between 1×10^4 to 1×10^5 cm^{-2} [41]. It was stated

that these dislocations were generated through "melt entrapment" caused by "wing" growth along the dendrites [45]. The growth of dendrites is also dependent upon the curvature of the solid-liquid interface during growth.

The EBIC measurements on Web materials showed that there was a high density and variety of dislocations which resided in the twin boundaries. The specimens were either polished parallel to the surface until the twin boundaries were located, which was approximately 1 μm below the surface, or at a shallow angle to the growth surface so that twin boundaries would intersect the polished surface [41]. Both hexagonal dislocation networks, which consist of near screw a/6 <112>dislocations [41], and long straight dislocations (thought to be Lomer-Cottrell locks) were observed [41]. Large area stacking faults of the Lomer-Cottrell type were also observed lying in (111) planes parallel to the surface [45]. Generally grain boundaries were not observed in dendritic Web materials; however, it was stated that "too high a growth rate can lead to grain boundaries" [45:569].

Analytical Techniques

There are many different analytical techniques for investigating the electrical and microstructural properties of polycrystalline silicon solar cell devices. The research previously described in this review has utilized etching techniques, electron channeling, EBIC, SEM, TEM, HVTEM and DLTS. There are many new high speed techniques for

characterizing silicon solar cells such as by silicon-electrolyte-contact (SEC) [46] or by real-time x-ray diffraction [47].

In the present investigation, the objective was to develop an overall characterization of the samples and then to select areas of interest for subsequent in-depth analysis. To accomplish this goal, three analytical techniques were selected: electron channeling, EBIC and TEM. Electron channeling was used to determine the crystallography of a sample. The EBIC technique is one of the few techniques which can qualitatively measure the "local" electrical properties of a device. The electron channeling and EBIC results were combined to determine any correlations between the crystallography of a sample and the corresponding electrical properties. The TEM was then used to investigate the effects of microstructure on the electrical properties of a sample. Thus by using this combination of analytical techniques, the effects of crystallography and microstructure on the electrical properties of the overall sample could be investigated.

Electron Channeling

The electron channeling technique is done on an SEM utilizing backscattered electrons. A very thorough description of this technique is given in the paper by Joy, Newbury and Davidson [48]. Briefly, this technique is based upon the observation that the probability of an electron being backscattered depends on how close it approaches the nucleus of the atom from which the electron is scattered [48]. Therefore, if the incident beam is stationary and travelling parallel to a set of planes, there will be much less backscattering of electrons

than if the incident beam is moved about (see Figure 3). If it is assumed that "the electron flux from the incident beam travelling through the crystal lattice can be mathematically represented as a number of standing waves known as Bloch waves, each of which has the periodicity of the lattice" [48:R81] and that the "square of the amplitude of a Bloch wave at any point represents the probability of finding an electron there" [48:R81].

A Type I Bloch wave describes the incident beam running parallel to the centers of the atoms which gives a strongly backscattered signal. A Type II Bloch wave describes the incident beam running parallel to half way in between atom centers or half a lattice spacing which gives a weakly backscattered signal. The ratio of Bloch wave I to Bloch Wave II is determined by the angle between the incident beam and the lattice. Although the sum of the intensities of the two Bloch waves must remain constant, the ratios of the intensities can vary and this in turn will alter the amount of backscattered signal. Thus bands of contrast will be formed from planes normal or nearly normal to the surface (see Figure 4). A pattern then develops which mimics the crystal. Each line in the pattern corresponds to a particular (hkl) plane, the width of each band will be twice the appropriate Bragg angle for the set of lattice planes from which it comes and the angle between the bands will be the angle between the corresponding sets of lattice planes [48]. The incident beam can be scanned over the sample to give electron channeling contrast maps or rocked about a point to give selected area electron channeling patterns (SACP). The information

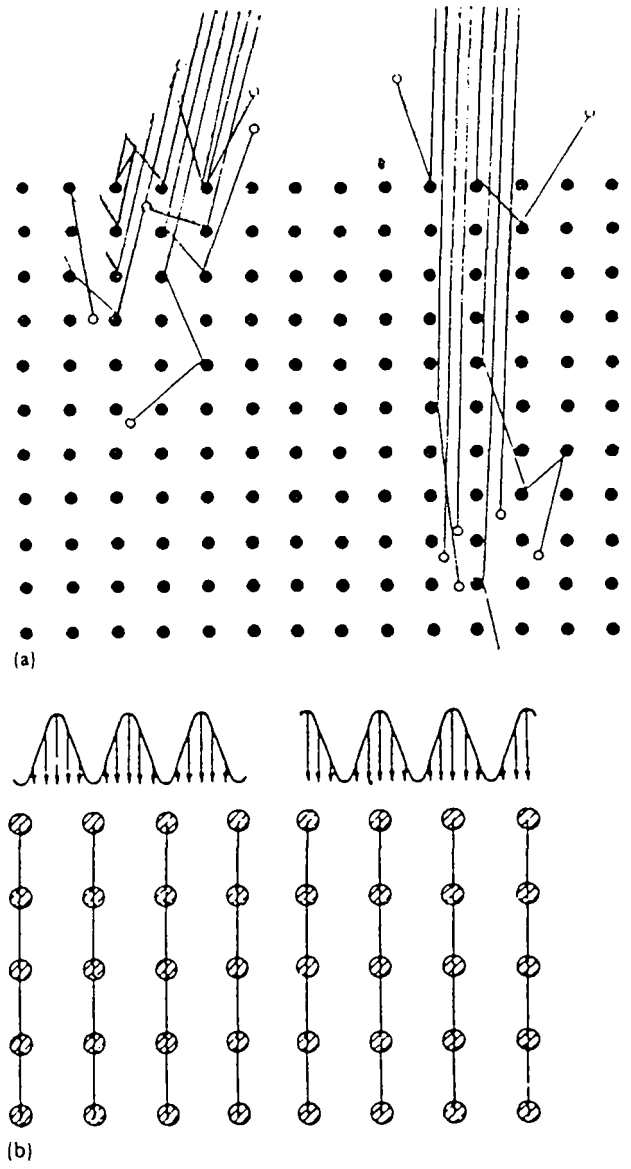

Figure 3. (a) Schematic showing the variation in the backscattered signal by a change in the angle of the incident beam. (b) Schematic of a Bloch Wave Type I and a Bloch Wave Type II, respectively [48:R82].

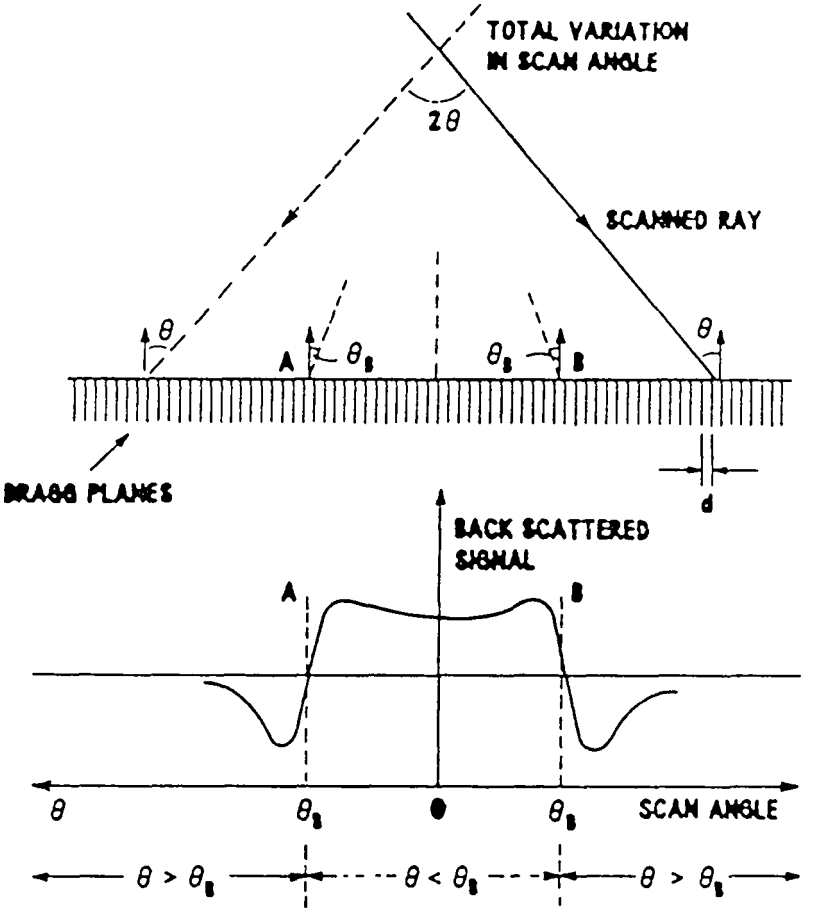

Figure 4. Schematic showing the formation of bands of contrast from the backscattered signal [48:R82].

obtained from SACP is analogous to a more conventional electron diffraction pattern.

The purpose of using the selected area electron channeling technique was to determine the orientations of the surface normals and the growth directions of the grains and also to try to determine any correlations between the crystallography of a sample and the electrical effects. Electron channeling contrast maps can also "reveal contrast from grain and subgrain structures, twins from deformations of the lattice due to cold working, and even contrast from the lattice bending which occurs around individual lattice defects" [48:R83].

Some of the major limitations to this technique include specimen thickness, specimen topography and beam diameter. Electron channeling is basically a surface technique where the contrast is created in a relatively thin surface layer (less than 100 nm thick) [48]. It is also a weak contrast technique and thus surface roughness must be minimized without inducing extensive plastic deformation. Finally, channeling contrast information is developed from an area of irradiation which is larger than the beam diameter. This large area of irradiation limits the type of information which can be acquired with this technique.

Electron Beam Induced Current

The EBIC technique is also available on a suitably equipped SEM. This method relies upon the creation of electron-hole pairs produced by the collision of primary electrons with valence electrons in the material [16]. If an electric field is present in the material, such

as from a charge gradient in the depletion region of a p-n junction or some form of an induced junction, then the electron-hole pairs or mobile charge carriers will be swept out of the depletion region (see Figure 5). The mobile charge carriers create a measureable current which is sent to a preamplifier and is seen as a signal on a CRT screen (see Figure 6). At this point, the signal seen on the CRT screen is uniform since the same number of charge carriers are being generated. The generation factor of mobile charge carriers in the EBIC technique is a function of the beam energy and the material being bombarded [16]. Assuming that the beam energy remains relatively constant, then the competing process for the collection of charge carriers would be carrier recombination, which is a material related process. Carrier recombination often occurs by one of the carriers being trapped at a specific point in the crystal such as at a grain boundary or defect [16]. This carrier recombination would create a short circuit current (I_{SC}) and would be seen as a black or dark area on the CRT screen. Therefore, with this technique electrically active defects are detected on the CRT screen as dark areas whereas areas of favorable electrical response are seen as light areas on the CRT screen. The use of the EBIC technique is then preferable for developing a picture of the "local" electrical characteristics of a device rather than the external device characteristics as determined by I-V measurements.

The major limitation of the EBIC technique used in this investigation is the qualitative nature of the results from it. "Factors such as the excitation geometry, carrier diffusion, carrier recombination

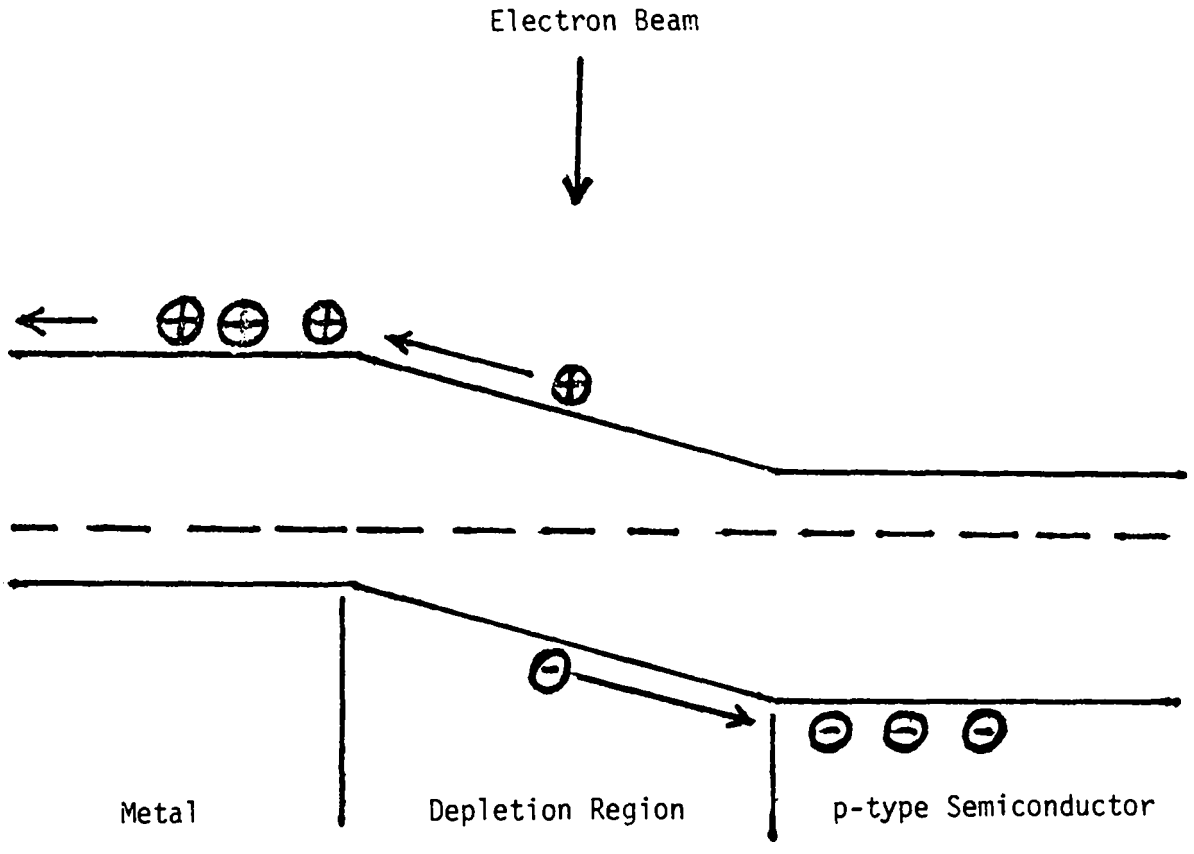

Figure 5. Schematic of an incident beam hitting the depletion region and the subsequent creation of electron-hole pairs.

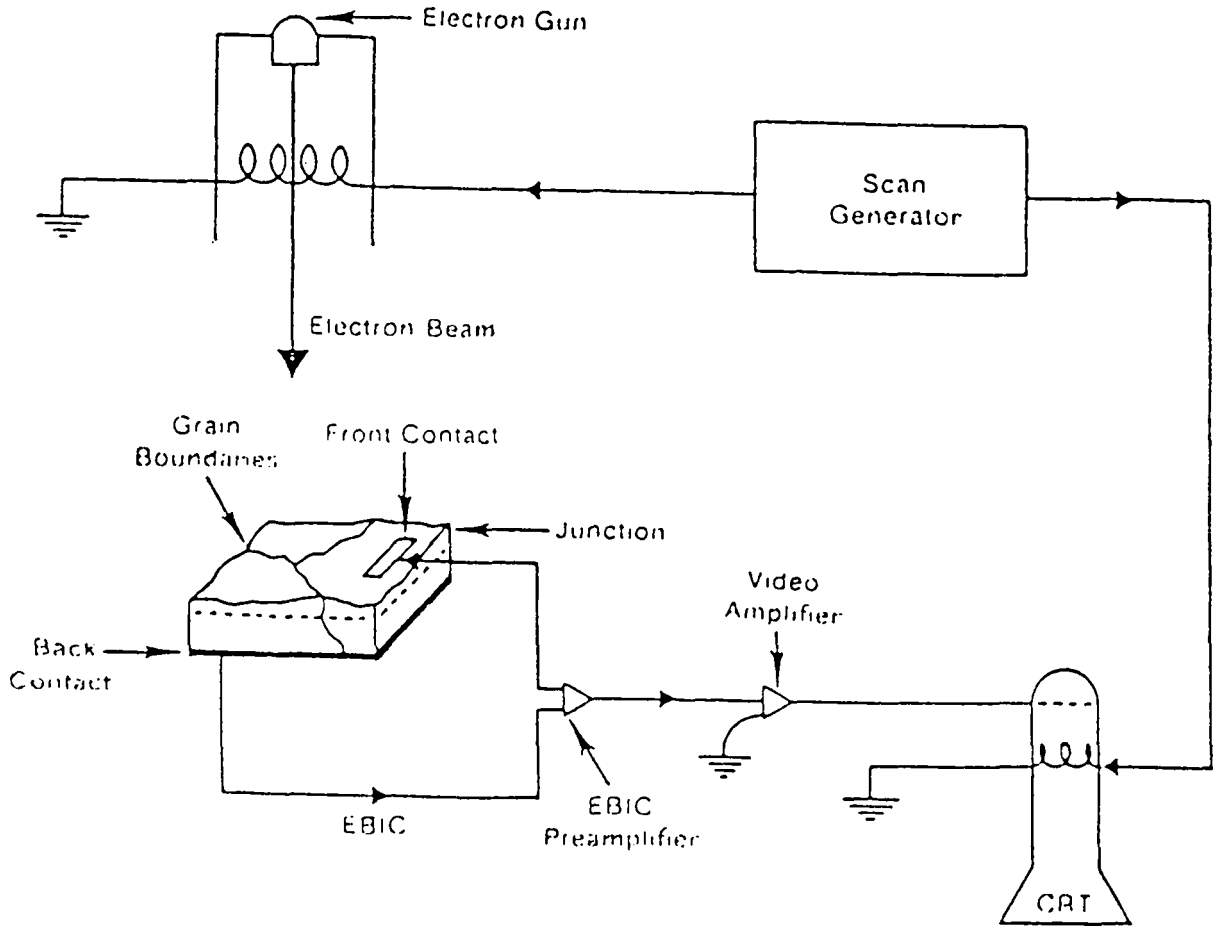

Figure 6. Schematic of the SEM setup for EBIC [16:17].

and barrier geometry involved in the current measurement make the quantitative interpretation of EBIC experiments difficult" [19:1172]. However, in response to this problem several theoretical models have been developed to try to quantify the EBIC results. These models account for the influence of several grain boundaries [49], the generation depth by the electron beam [50], the current decay due to the distance from the probe [50], etc. In light of these discrepancies, the EBIC results in this investigation were purely qualitative.

Transmission Electron Microscopy

Extensive literature has been published on transmission electron microscopy [51-53].

One of the main reasons for using this technique was to image microstructural defects at a higher resolution (about 2 Å) than is capable with an SEM (50 Å). The second reason for using EBIC/TEM as opposed to STEBIC/STEM (Scanning Transmission Electron Beam Induced Current/Scanning Transmission Electron Microscopy) was to analyze the overall sample as opposed to discrete areas. Also for STEBIC/STEM a thinned specimen must be prepared first before analysis and the condition of the actual sample before possible alteration of microstructure from TEM preparation techniques is unknown.

One of the major limitations in using the EBIC/TEM combination is the loss of an exact correlation between an electrically detrimental defect seen with the EBIC technique and the corresponding microstructural defect imaged in the TEM [54]. As stated earlier, the incorporation of microstructural defects from TEM specimen

preparation techniques can also cause confusion with the correlation of electrical and microstructural defects. Another limitation of the TEM technique is the small sample size, only a relatively small area around the hole of each disc can be analyzed. However, the EBIC/TEM analysis can be more characteristic of the sample as a whole when many discs are analyzed.

CHAPTER 3
EXPERIMENTAL PROCEDURE

Introduction

General Mode of Operation

The modes of operation for analyzing both the ESP and the LASS materials were very similar. The differences depended on the condition of the received material.

The ESP material was received as an already fabricated device, therefore electron channeling was not studied. An EBIC montage was developed and from this montage, areas of interest were selected for TEM analysis.

Discs, three millimeters in diameter, were cut and EBIC pictures were taken of each disc. The discs were ground, polished, dimpled and ion milled. Then TEM analysis was done.

The LASS material was received in the raw state. The samples were mechanically lapped, chemically polished and then electron channeling was done. The samples were then chemically cleaned and an aluminum layer was evaporated on one side of the sample and a gold layer on the other side. The same procedure as previously described for the ESP material was then followed. A flow chart of the mode of operation for these two materials is shown in Figure 7.

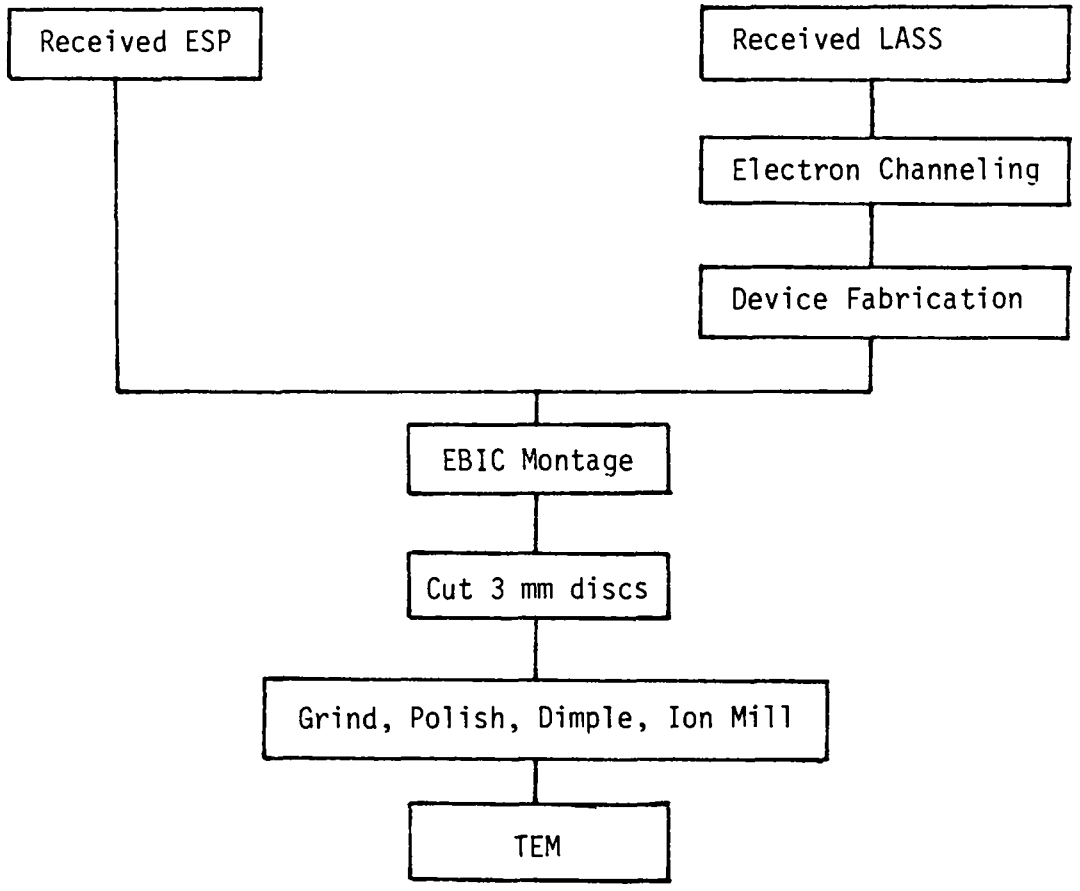

Figure 7. Flow chart of the mode of operation followed in this investigation.

Materials

Silicon sheets from two different fabrication techniques were investigated. One is ESP which is a horizontally pulled, high quality sheet technique. The other is LASS which is a vertically pulled, high throughput technique.

The ESP sample was SERI number R101, 113-2A. The overall size of the sample was approximately 6 cm x 4 cm. The sample was cut into four sections using a Struers Accutom saw. Three of the sections were then cut in half for easier handling during EBIC analysis. In most cases, the ESP was thinner on both sides with a thick section slightly offcentered to the right, as observed from the top surface (see Figure 8). During fabrication, the thickness of the sheets can vary from 110 μm to 1100 μm, depending on the hot zone temperature and the pull speed. This sample (R101) was pulled at an average rate of 15 mm/min and the thickness of this sample ranged from 230 μm to 500 μm with an average of 300 μm. The specimen thickness was measured on a light microscope using a short focal length objective lens and focusing the top and bottom surfaces on a calibrated stage.

The LASS sample was also initially 1.5 cm x 3 cm. However, this sample was tapered only on one side (see Figure 9). The thickness of this sample ranged from 715 μm to 1100 μm with an average of 900 μm, as measured by the microscope technique previously described. Thus, the LASS sample was roughly three times thicker than the ESP sample. The topography of the LASS sample as seen by the Nomarski photographs (see Figures 10-11) was typical of the random dendritic structure as opposed to the twin stabilized or parallel dendritic structure.

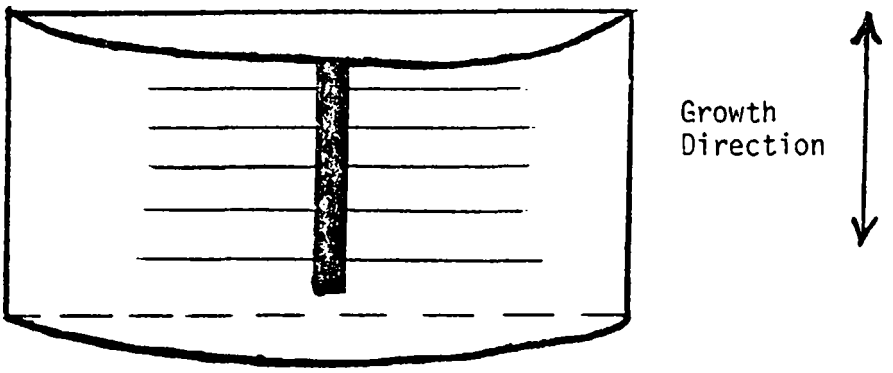

Figure 8. Schematic of the ESP sample.

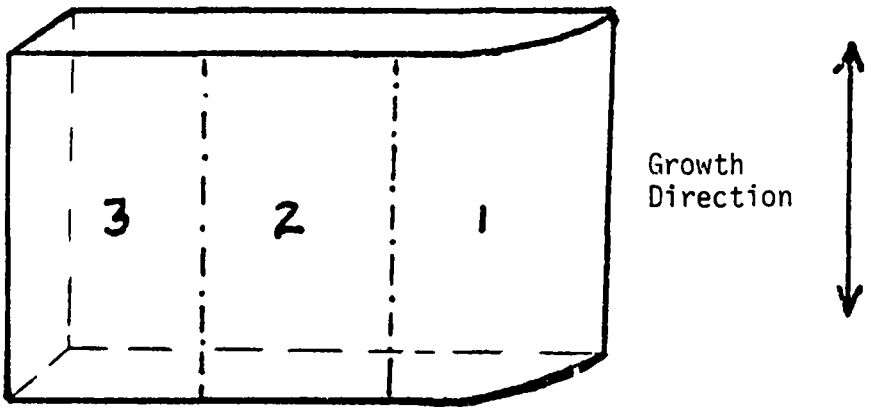

Figure 9. Schematic of the random dendritic LASS sample.

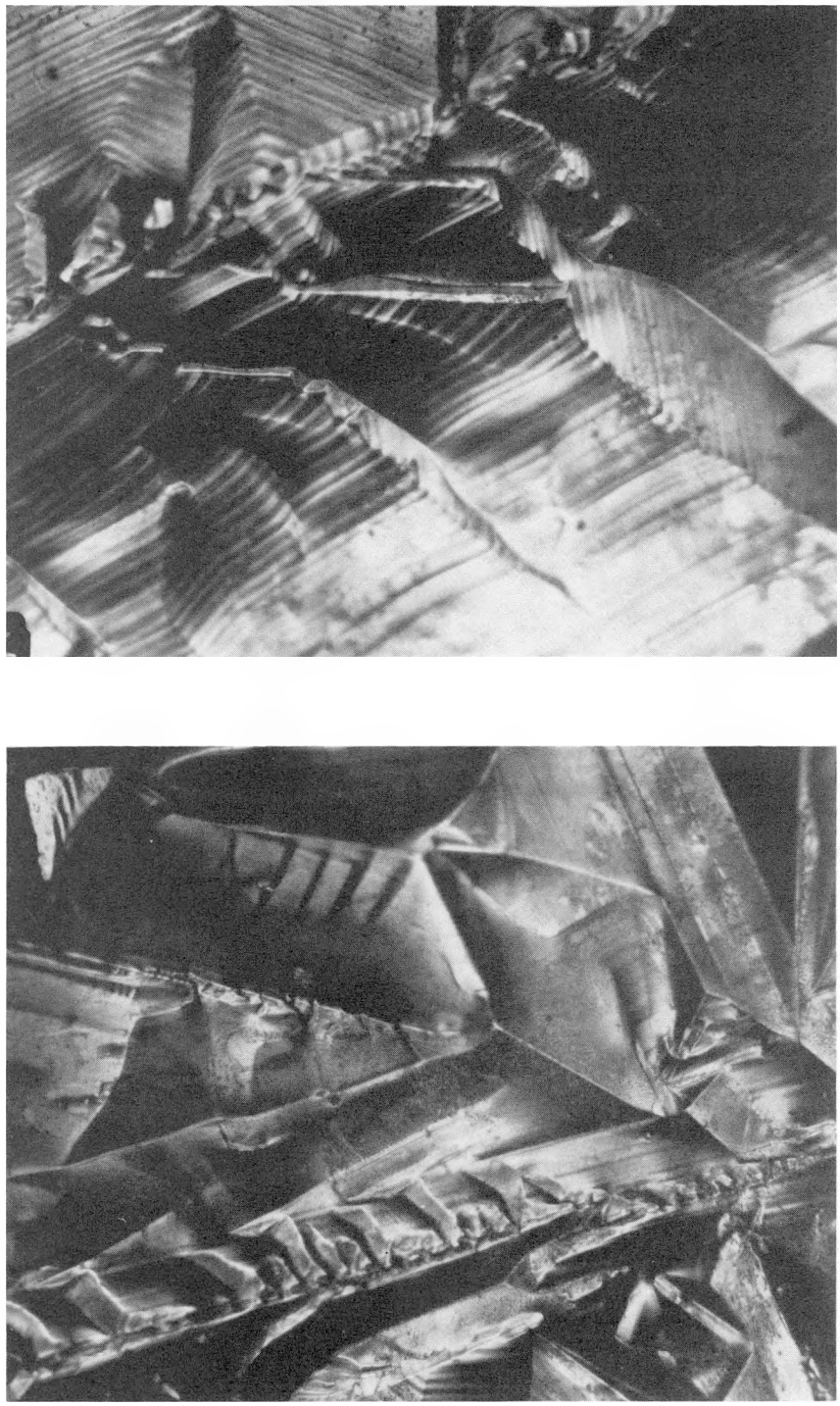

Figure 10. Two Nomarski photographs showing the rough surface topography characteristic of random dendritic LASS material (100X).

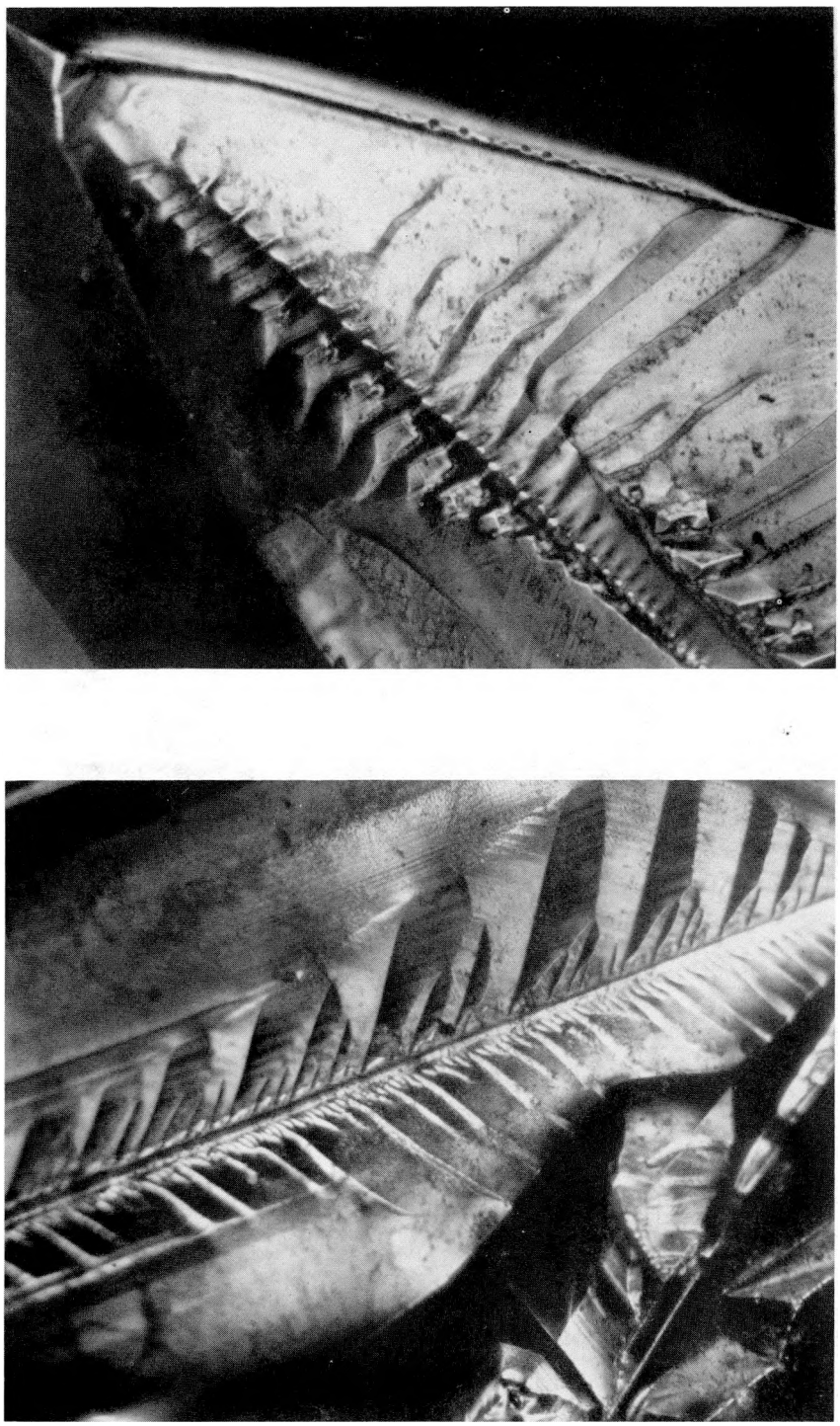

Figure 11. Two Nomarski photographs showing the dendritic growth structure characteristic of random dendritic LASS material (100X).

Device Fabrication

The ESP samples were received as fabricated devices from SERI. Generally, their procedure for device fabrication was to start with ESP silicon sheets doped with boron to produce a 1 Ω-cm resistivity. The surface oxides were removed from the samples by immersion in hydrofluoric acid and then chemically polished in a solution of HNO_3/CH_3 COOH/HF (6:1:1) for two minutes. The samples were then placed in a furnace with a $POCL_3$ atmosphere for ten minutes to diffuse a phosphorous coating on their surfaces. Following this treatment a 500 Å layer of titanium or aluminum was vacuum evaporated on the top surface to form a Schottky contact and a layer of aluminum was evaporated on the back surface. Contact wires were placed on the sample and the sample was annealed at 450°C for five minutes.

The LASS samples were fabricated into solar cell devices in-house. Device fabrication began with LASS samples that had been doped with boron to produce a 4 Ω-cm resistivity. The sample was first cut into three pieces 1 x 1.5 cm using a Struers Accutom saw. Samples one and two were used for EBIC and TEM work. Sample three was prepared for SAEC and EBIC work.

Samples one and two were first cleaned and polished using a standard wafer cleaning and polishing technique (see Appendix). The samples were then mounted on glass slides using adhesive tape on the corners of the samples. Pieces of 99.9985% pure aluminum wire were placed in a tungsten wire basket. A 670 Å layer of aluminum was then vacuum evaporated onto the samples to form a Schottky contact.

The samples were reversed and remounted on the glass slides. A piece of 99.9985% pure gold was placed in a molybdenum boat. An 820 Å layer of gold was evaporated on the samples to form an ohmic contact. The evaporator setup is shown in Figure 12.

Sample three was first mechanically lapped on both sides using 60 μm, 15 μm and then 5 μm silicon carbide lapping paper. The sample was then cleaned and polished by the standard wafer cleaning and polishing technique. Electron channeling was then performed on the sample. Sample three was subjected to the procedure described for samples one and two.

Analysis

Three analytical techniques were used in this investigation: Electron Channeling, Electron Beam Induced Current and Transmission Electron Microscopy.

Electron Channeling

Electron channeling was carried out on a JEOL JSM 35C scanning electron microscope with a G. W. Electronics Model 130 backscattering detector and electronic (absorbed current) monitor. The sample was mechanically lapped and chemically polished, as previously described. Electron channeling patterns and the corresponding scanning electron micrographs were taken of the overall specimen as well as of each grain in a designated area. From these data, a unit triangle map was developed. The scanning micrographs were used to identify grains

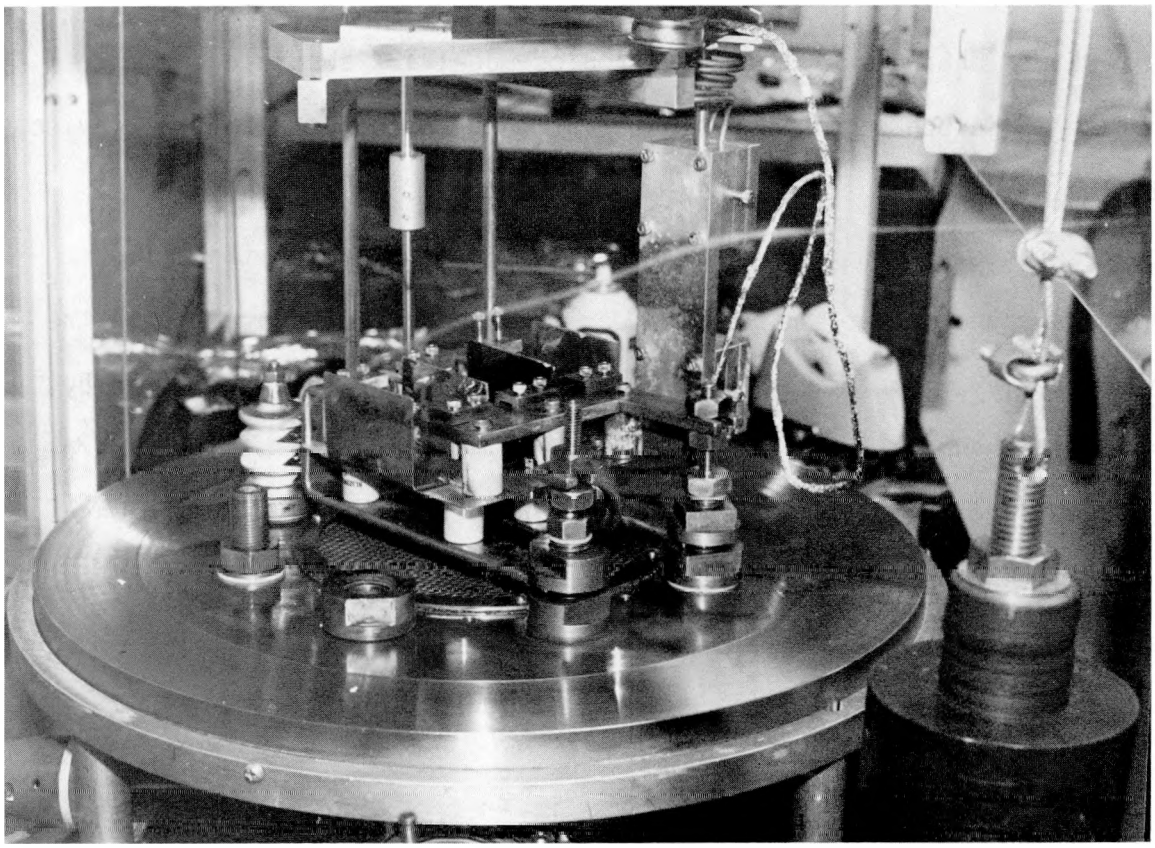

Figure 12. Evaporator setup used in this investigation.

of differing crystallographic orientation and to correlate this information with the EBIC data.

Electron Beam Induced Current

Electron Beam Induced Current measurements were done at 25 kV on a JEOL JSM 35C with a G. W. Electronics Model 103 absorbed current monitor. Carbon paint was used to form a base contact from the device to the stage. The stage was placed in the EBIC holder which is a gold-ceramic 18-pin flat pack device. A tungsten probe with a 1.6 mm tip was connected to the EBIC holder to make a front contact with the aluminum layer of the device. The EBIC holder was then connected by a 20-pin connector to a ground box which was connected by a standard BNC cable to the G. W. preamplifier. The vacuum on this system was normally in the pressure range of 10^{-5} Torr and was created by a standard oil diffusion pump.

Transmission Electron Microscopy

Transmission Electron Microscopy was done on a JEOL 200CX. Three millimeter discs of selected areas were cut out of the sample using a Gatan Model 601 Ultrasonic Disc Cutter. The LASS discs were then mechanically lapped with a Gatan Disc Grinder, Model 623, to a thickness of about 200 μm on 60 μm, 40 μm, and then 5 μm silicon carbide lapping paper. The ESP discs were not ground on the lapping paper since they were so fragile and already quite thin. The thicknesses of both the LASS and the ESP discs were measured with a light microscope using a short focal length objective lens and focusing on the top and bottom surfaces

on a calibrated stage. The orientation of the discs with the EBIC photos was marked. Initially a spot of epoxy was used to mark the orientation. This method was not very effective and the epoxy polymerized in the ion miller. It is known that the heating necessary to set the epoxy may alter the microstructure [16]. A felt tip pen was then used to initially mark the orientation and was followed up by carbon or silver paint for identification in the STEM mode of the TEM. The silver paint was actually easier to identify in the STEM mode than the carbon paint. The three millimeter discs were then polished and dimpled on a VCR Group Dimpler. The samples were mounted with the aluminum side up, reduced in thickness by 40 μm with three micron diamond paste, dimpled to 30 μm with one micron diameter diamond paste, and polished with Syton polish for a few minutes. The samples were then thinned in a Commonwealth Scientific Ion Miller from only one side with an argon beam. The vacuum in the ion miller was created from a roughing pump-turbo pump combination and was in the pressure range of 10^{-5} Torr.

CHAPTER 4
RESULTS

The results from this investigation include electron channeling results on the LASS material, EBIC results on both the ESP and LASS materials and TEM results on both the ESP and LASS materials.

Electron Channeling

Extensive electron channeling studies have been done by SERI on ESP materials and therefore were not done again. However, these studies were used for comparison and as a guide for electron channeling studies on the LASS samples.

The electron channeling results from this investigation showed that 81% of the surface normals were located less than 5° off of either the [113], the [233], the [015] or the [2 7 16] poles (see Figure 13). The distribution of these grain orientations in the sample were: 24% located less than 4.5° off of the [113] pole, 19% located less than 2.5° off of the [233] pole, 19% located less than 2° off of the [015] pole, and 19% located less than 1° off of the [2 7 16] pole (see Table 1). It was interesting to note that many of the channeling patterns taken from different parts of the sample tended to be oriented almost, if not exactly, the same.

For comparison with other research, 43% of the grains were oriented less than 27° off of the [111] pole, 48% of the grains were oriented less than 23° off of the [001] pole, 10% of the grains were oriented less than 11° off of the [011] pole.

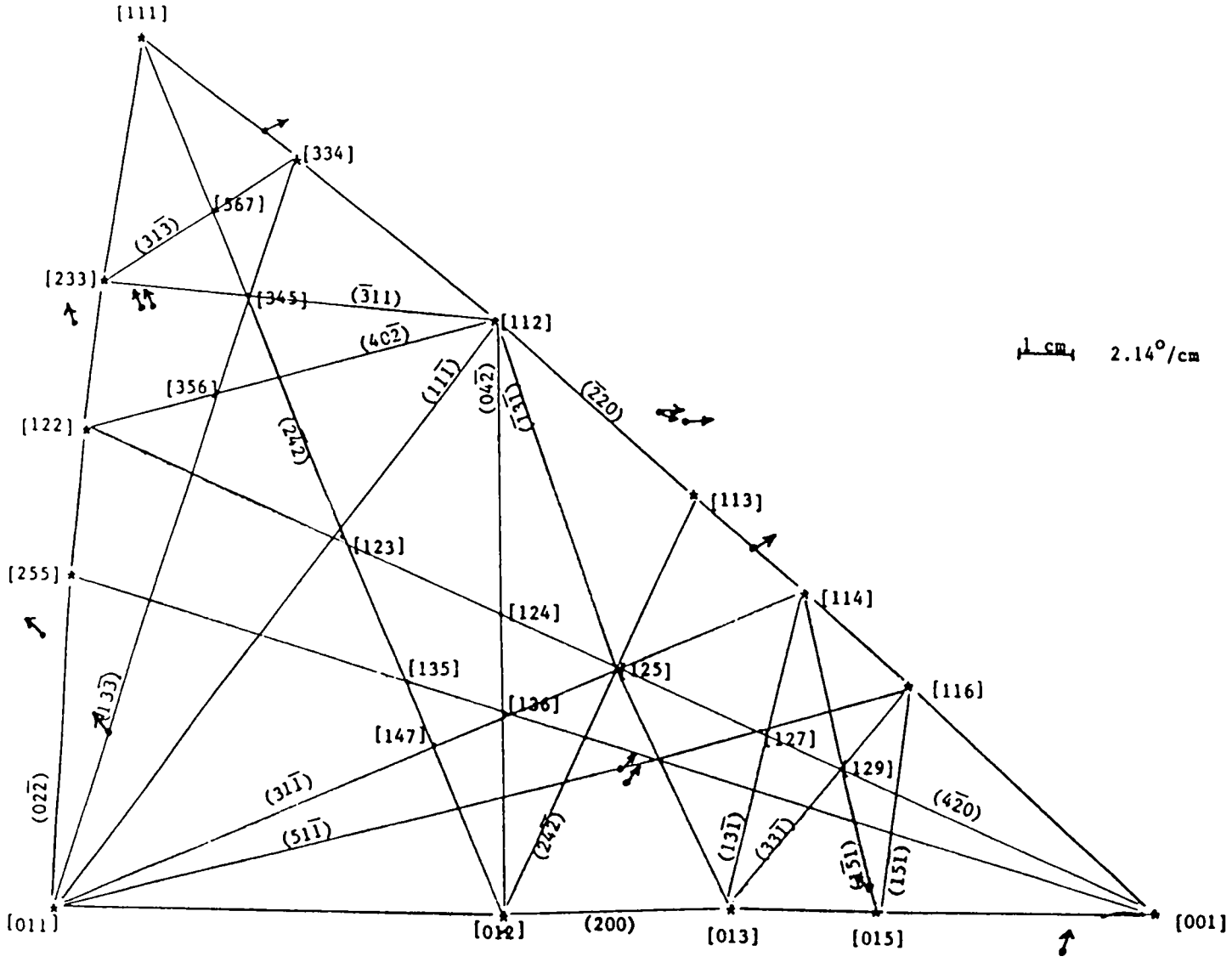

Figure 13. Electron channeling unit triangle map of the random dendritic LASS material.

Table 1

Summary of LASS Electron Channeling Results

Pole	[113]	[2 7 16]	[233]	[015]	[001]	[255]	[334]	Totals
Distance from pole (degrees)	3.5° 3.0° 2.4°	0° 0.5°	2.4° 1.9° 2.4°	1.1°	4.3°	6.2° 2.8°	1.9°	--
Number of Points	17	13	11	4	1	2	1	49
Number of Grains	5	4	4	4	1	2	1	21
% of Points <5° Off of Pole	35%	27%	22%	8%	2%	2%	2%	98%
% of Grains <5° Off of Pole	24%	19%	19%	19%	5%	5%	5%	96%
Degrees from [111]	27.0° 26.1°	--	10.9° 11.7°	--	--	--	6.2°	--
Degrees from [011]	--	--	--	--	--	7.3° 10.7°	--	--
Degrees from [001]	21.8°	22.5° 22.3°	--	11.8°	4.3°	--	--	--
% of Grains near [111]	19%	--	19%	--	--	--	5%	43%
% of Grains near [011]	--	--	--	--	--	10%	--	10%
% of Grains near [001]	5%	19%	--	19%	5%	--	--	48%

The growth or pull directions of all the grains in this sample were parallel to the {211} family of planes by ± 10° or less.

Electron Beam Induced Current

In general, the qualitative EBIC results showed that the overall electrical response of both the ESP and the LASS materials were fairly similar. Visually both EBIC montages seemed to have the same amount of contrast. The SEM was set up similarly for both materials. A tungsten filament was used with similar settings for the objective lens, condenser lens, apertures and current on the absorbed current monitor which read between 10^{-6} to 10^{-7} amps. However, there was quite a difference in the patterns of poor electrical response between these two materials.

Edge Supported Pulling

The EBIC montage of the ESP material showed long, linear bands of poor electrical response (see Figure 14). The montage seemed to be made up of five different regions of EBIC response which tended to be repeated through the width of the sample. One region (I) was composed of a set of linear, parallel bands angled between 90-105°. Another region (II) was composed of cross-hatched lines at approximately 65° angles to each other. A third region (III) was composed of non-angled, linear, parallel bands. A fourth region (IV) was composed of knarled bands (see Figure 15). In one of the knarled regions, the dark knarled bands seemed to emanate from a small impurity or stone,

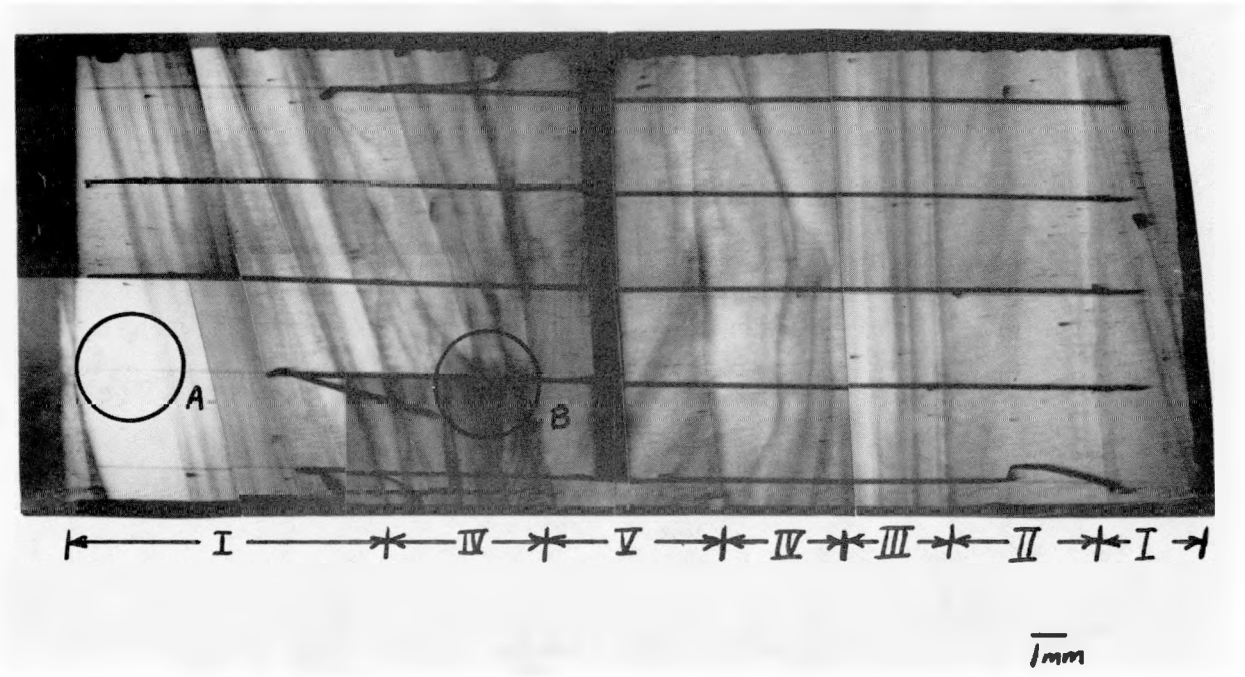

Figure 14. EBIC montage of an ESP sample at 25 kV (10X). This montage shows regions of angled, parallel lines (I); cross-hatched lines (II); linear, parallel lines (III); knarled bands (IV); and the center (V). Circle A is characteristic of an area of good electrical or predominantly light EBIC response. Circle B is characteristic of poor electrical or relatively dark EBIC response.

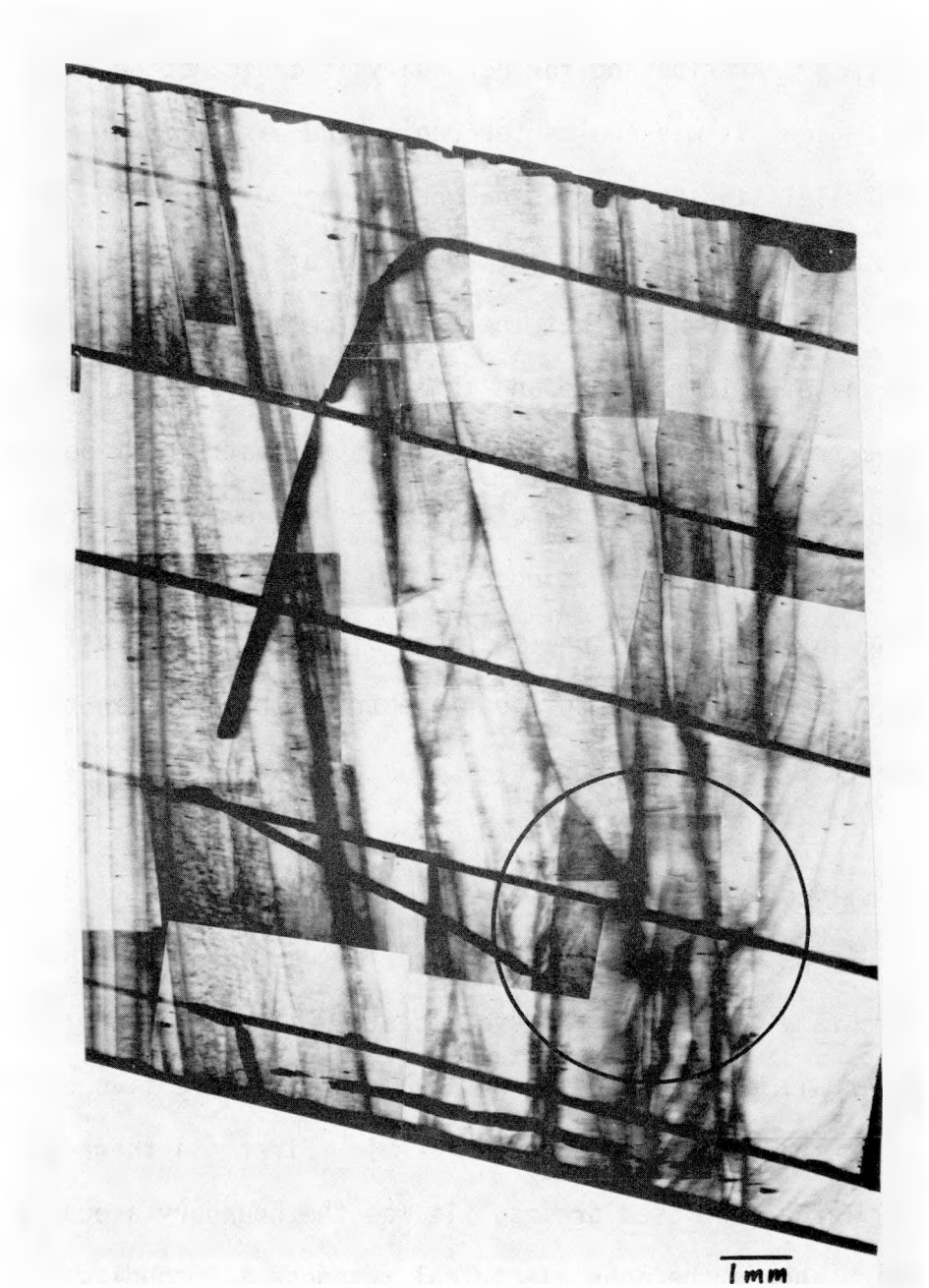

Figure 15. EBIC photograph of one of the knarled regions (IV) in the montage of Figure 14. The marked area shows a perturbation in the knarled bands (25X).

as known in glass melting. Unfortunately, the sample with this area broke in TEM preparation and further analysis could not be done on it. The fifth region (V) was the center region and was a mix of angled, linear, parallel lines and cross-hatched lines. A dark band was noticed at the pinnacle of the thick section of the sample (see Figure 16). It was thought that there might be a correlation between these regions of EBIC response and thickness, however, this did not prove to be true. It was also noticed that the pattern of perturbations in the surface topography of the material seemed to correlate with the EBIC pattern. It was observed that in 13 of the 21 samples which broke in TEM preparation, the line of fracture seemed to be along the corresponding band of poor electrical response in the EBIC photographs.

Low Angle Silicon Sheet

The EBIC patterns for the LASS material varied quite a bit from one EBIC montage to another, however, certain similar trends did seem to appear in all three samples. Basically, there were five different types of EBIC patterns (see Figures 17-19). First (I) there were a few fairly large, enclosed grains. It was the boundary around these grains which showed the poor electrical response. Secondly, (II) there were a few sets of long, linear bands which ran parallel to each other. These sets of bands were usually less than 35° from another set, although this angle varied from set to set. Thirdly, (III) there were a few regions of numerous rows of fairly short, parallel lines (see Figure 19). Also, (IV) there were many small enclosed grains usually

Figure 16. EBIC photograph of half of the center region (V), the knarled region (IV), and the linear, parallel lines (III) (20X). Note the dark band at the pinnacle of the thick section of the sample.

Figure 17. EBIC montage of random dendritic LASS sample number three. This sample was also used for electron channeling. In this montage circle (I) shows a rectangular grain, circle (II) shows part of a set of long, linear bands, circle (IV) shows small enclosed grains, and circle (V) shows some dislocation clusters.

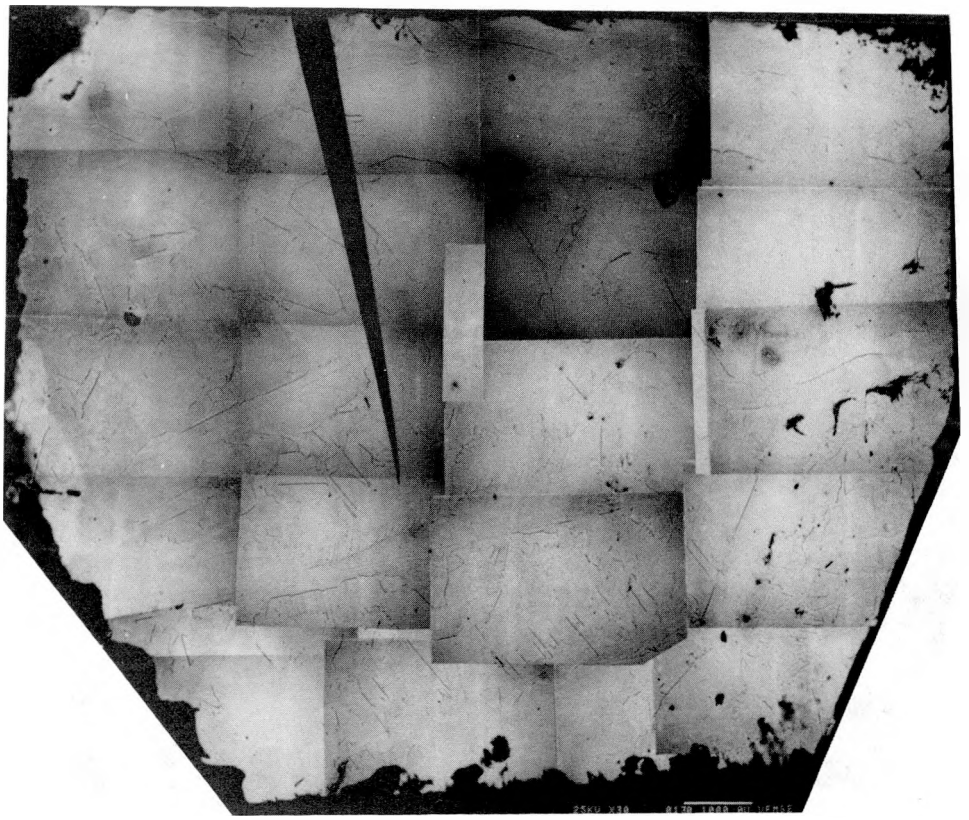

Figure 18. EBIC montage of random dendritic LASS sample number two.

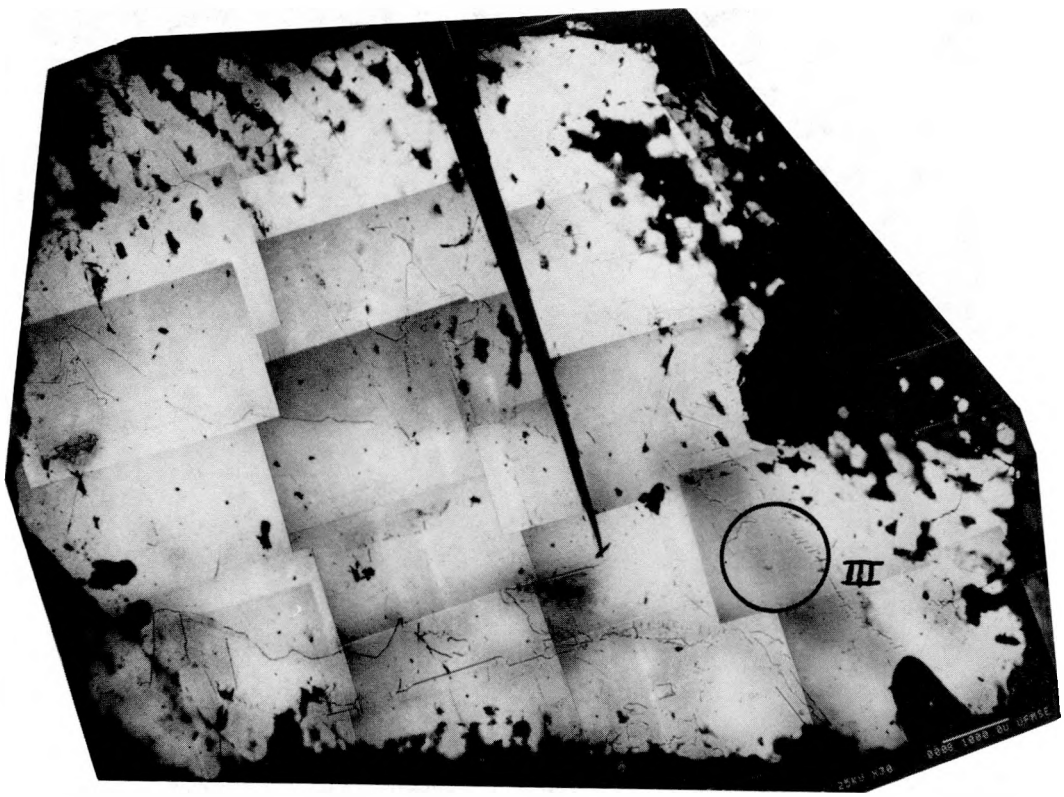

Figure 19. EBIC montage of random dendritic LASS sample number one. Circle (III) shows numerous rows of short, parallel lines.

about 0.4 mm^2 which looked similar to those described by SERI as polycrystalline silicon inclusions. Finally, (V) there were very small islands about 0.065 mm^2, usually along the sets of long, linear bands. These seem to be about half the size of the dislocation clusters described by SERI but appeared similar in appearance. It was interesting to note that certain topographical features seen in the SEM photographs (see Figure 20) were not seen in the EBIC photographs (see Figure 21). In the ESP material, the topographical and EBIC features did seem to correlate much more closely.

The effect of grain orientation on the electrical properties was analyzed by comparing the electron channeling and EBIC results. SERI reported that ESP material composed of the dominant grain structure with surface normals near the [011] direction and the growth direction parallel to the (111) plane gave less electrically active defects. The electron channeling and EBIC results of the LASS material were then superimposed on each other to try to determine this same effect. From Figure 21 it can be seen that there is no direct correlation between a grain of a certain orientation and its electrical properties in the random dendritic LASS material. However, it was felt that there could be a correlation between the dominant grain structure of the twin stabilized planar LASS, with surface normals oriented at [111], and preferable electrical properties.

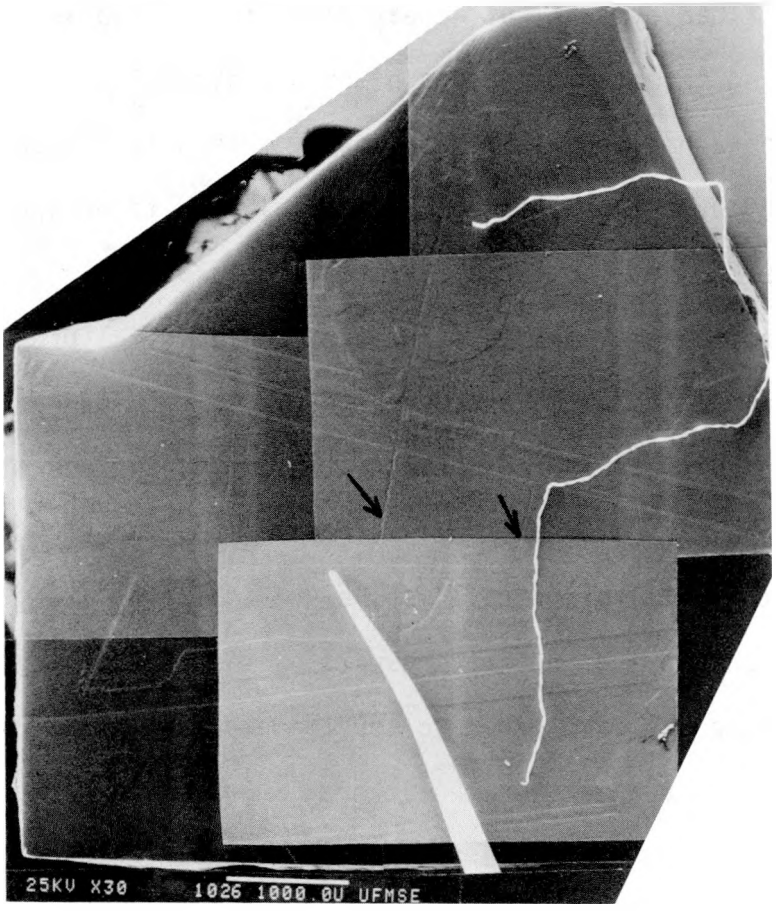

Figure 20. SEM topographical image of an LASS sample. Note that certain topographical features are not seen in the EBIC montage of Figure 21.

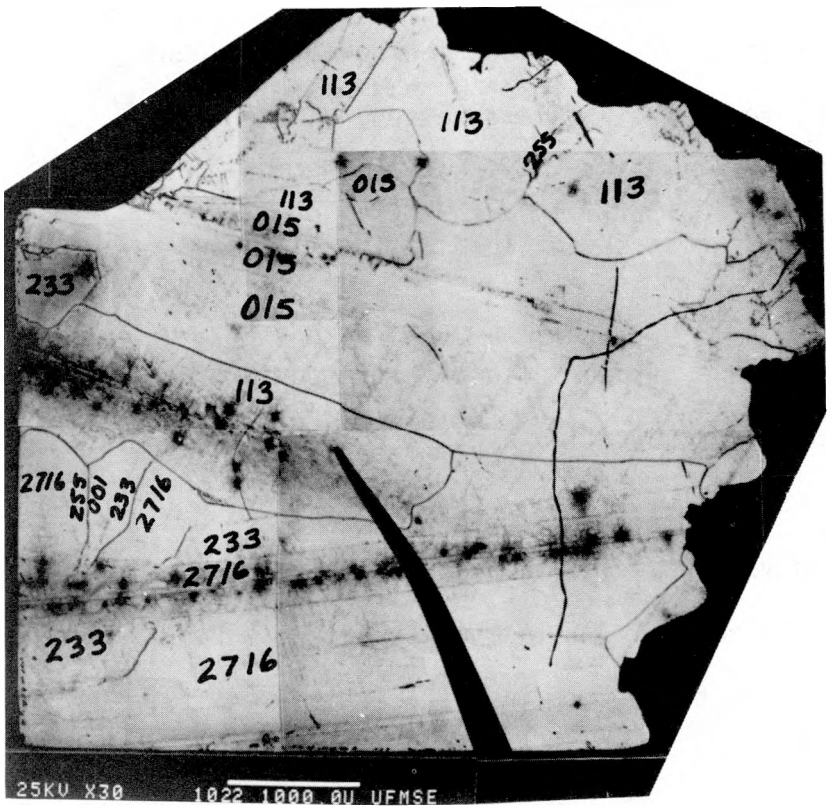

Figure 21. EBIC montage combined with the results of the electron channeling study.

Transmission Electron Microscopy

Edge Supported Pulling

The TEM results of the ESP samples showed the presence of stacking faults, twins and dislocations.

In the regions of good electrical or predominantly light EBIC response very few defects were observed. These areas of good electrical response were often surrounded by areas of poor electrical response containing stacking faults either in piles or singularly (see Figure 22).

In the regions of poor electrical response or areas of a relatively high concentration of dark EBIC, numerous defects running approximately parallel to each other were observed (Figure 23). These defects were observed to be stacking faults and twins which were piled up together. Dislocations were observed to be pinned to stacking faults but not to twins (see Figures 24-25).

Low Angle Silicon Sheet

The TEM results of the LASS material showed the presence of stacking faults, twins, grain boundaries, dislocations and precipitates.

The samples of overall good electrical or predominantly light EBIC response tended to have no observable stacking faults or twins (see Figure 26). However, dislocations and precipitates were observed in these samples. The size, shape and orientation of the dislocation tangles varied from sliver shaped, approximately 0.1 μm x 0.8 μm in size, to broad fan shaped tangles, approximately 0.3 μm x 1.8 μm.

Figure 22. Single stacking fault with pinned dislocations seen in an ESP sample (8,000X).

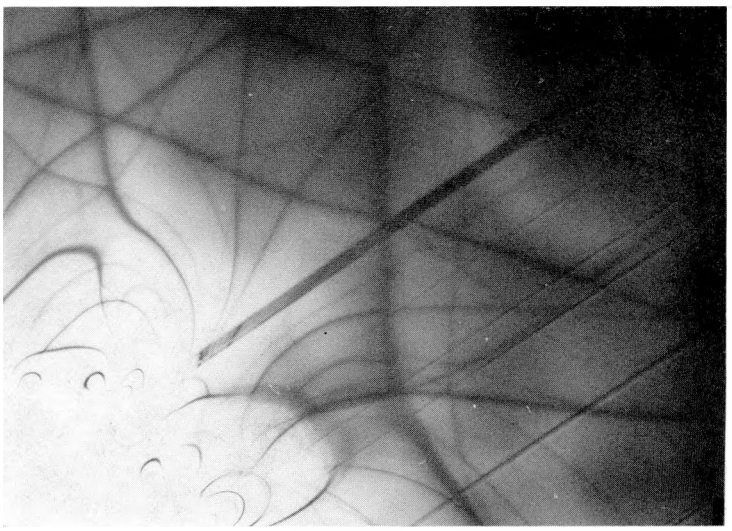

Figure 23. An ESP sample showing numerous twins and stacking faults running parallel to each other (10,000X).

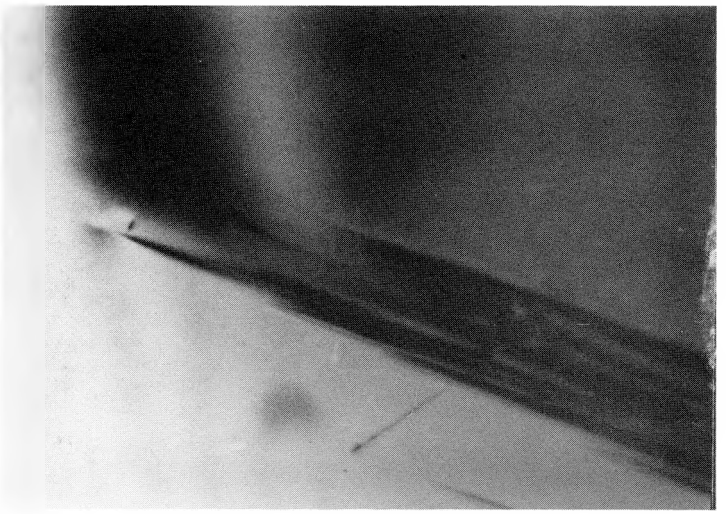

Figure 24. Stacking fault with dislocations pinned to it observed in an ESP sample (30,000X).

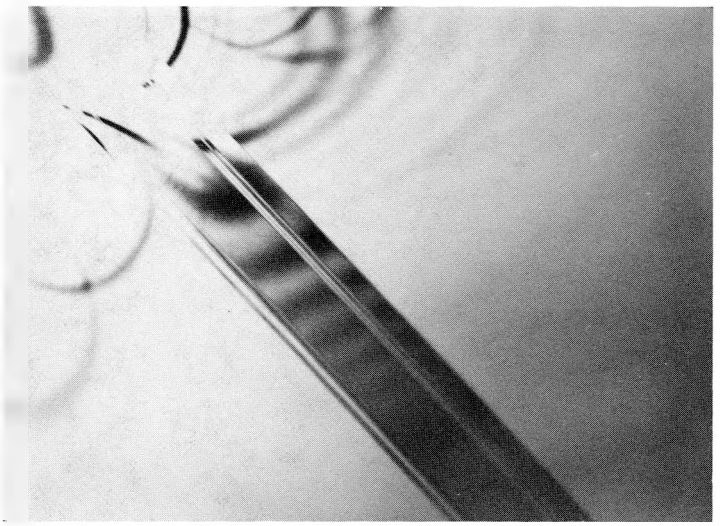

Figure 25. An ESP sample showing a twin with no observable dislocations pinned to it (15,000X).

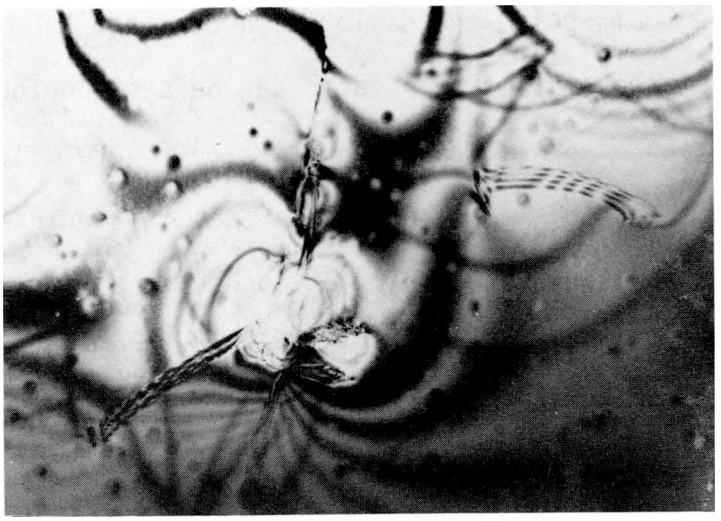

Figure 26. Typical area in a good EBIC response area of an LASS sample (15,000X).

The sliver shaped dislocation tangles were either alone, as in Figure 27, or conglomerated together, such as in the dogbone shape of Figure 29. The sliver shaped dislocations can be seen in each of the photographs of Figures 27, 29 and 32 at three different orientations and thus these dislocations are not predominantly orientation dependent. The dogbone shaped dislocation tangles appear to be a collection of three dislocation tangles connected together (Figures 29-30). By using dark field imaging with the streaks of the (220) spot near the [001] pole, the dislocation contrast is minimized and what appears to be small precipitates can be seen on the far ends of this combination of dislocation tangles (see Figure 31).

The fan shaped dislocation tangles seen in Figures 32-33 were oriented at a zone axis of [112]. Throughout the samples such fan shaped tangles were often observed with a zone axis of [112]. Figure 34 shows how the fan shape is enhanced by orienting on the (111) spot of the [112] pole.

The LASS samples of relatively poor electrical response also had dislocation tangles with precipitates similar to those found in the samples of overall good electrical response (Figure 35). However, the presence of grain boundaries, twins, stacking faults and lines of dislocation tangles were also observed.

A typical grain boundary is shown in Figure 36, oriented at a zone axis of [111]. Note that there are no dislocations, stacking faults, etc. near this grain boundary.

Twins were also present in these samples. Figure 37 shows a typical twin. Notice that there are no dislocations pinned to it.

Figure 27. Typical bright field photograph of a dislocation tangle shaped like slender slivers oriented at a [122] zone axis (20,000X).

Figure 28. Dark field photograph of the above dislocation tangle (20,000X).

Figure 29. Bright field photograph of a dogbone shaped dislocation tangle oriented near a [100] pole on the 220 spot (20,000X).

Figure 30. Dark field photograph of above dislocation tangle at the same orientation as above (20,000X).

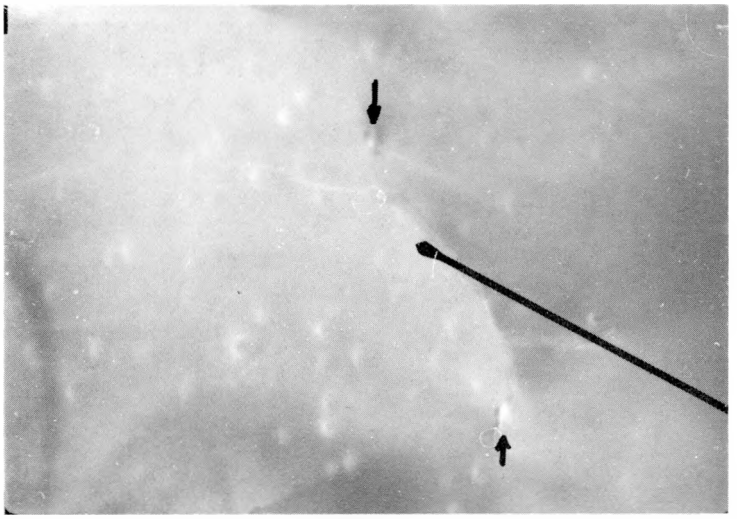

Figure 31. Dark field photograph of dislocation tangles seen in Figure 30 but oriented on the streaks of the 220 spot. Note the two precipitates on the far ends of the dogbone shape (20,000X).

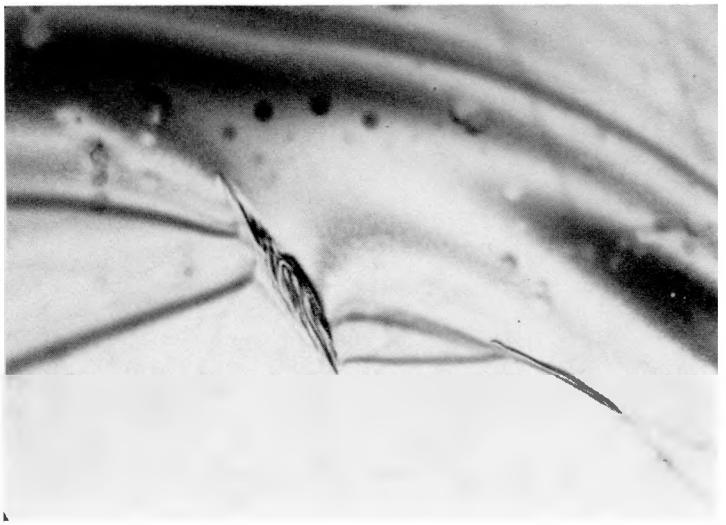

Figure 32. Fan shaped dislocation tangles imaged on the (220) spot of the [112] pole. The fan shape is almost invisible at this orientation (20,000X).

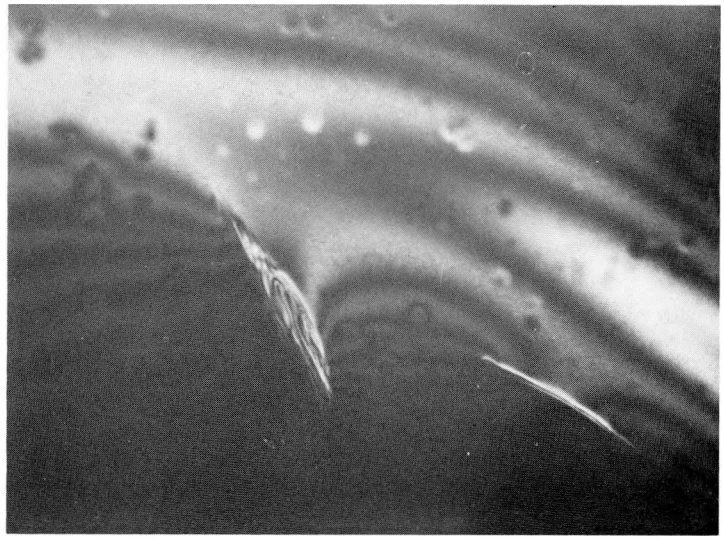

Figure 33. Dark field photograph of the fan shaped dislocation tangles seen in Figure 32 (20,000X).

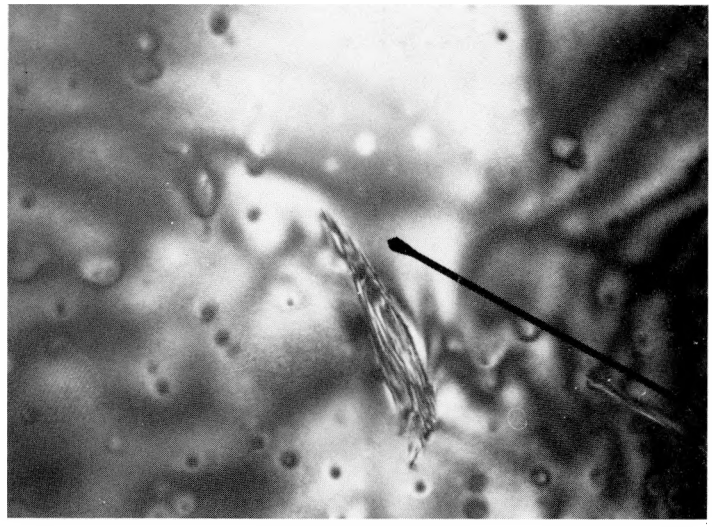

Figure 34. Dark field photographs of fan shaped dislocation tangles oriented on the (111) spot of the [112] pole. Note the enhancement of the fan shape at this orientation (20,000X).

Figure 35. Typical dislocation tangles found in the LASS samples (10,000X).

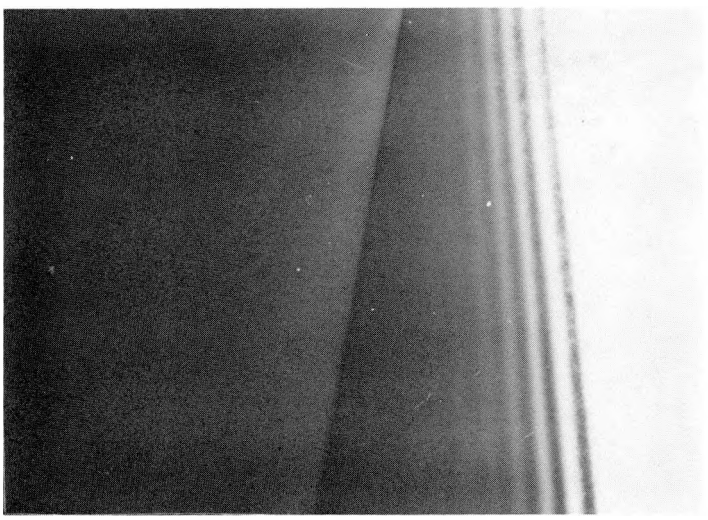

Figure 36. Typical grain boundary observed in the LASS samples oriented at [111] (50,000X).

Figure 37. A typical twin in the LASS material. Note that there are no dislocations pinned to it (15,000X).

Figure 38a shows a coherent twin boundary. Both sides of this twin boundary are oriented at zone axes of [001] but at 70° angles to each other, as can be seen in the diffraction pattern (Figure 38b). Notice that dislocations are pinned to this boundary.

Two types of stacking faults were observed: those emanating from an edge (Figures 39-40) and those contained within the sample (Figure 41a,b). The stacking faults emanating from an edge often had dislocations pinned to them or lines of dislocations located nearby. The stacking faults contained within the sample were similar in appearance to twins and no observed dislocations were pinned to them.

Lines of dislocations (Figure 42) were often located close to or actually crossing stacking faults. Lines of precipitates with dislocation tangles surrounding them were also observed (Figures 43-44). The lines of precipitates were most easily seen when oriented at a [112] zone axis, similar to the single precipitates with dislocation tangles previously described.

Quite frequently planar boundaries, such as those shown in Figures 45-49, were seen in the LASS samples. These were often observed oriented near a [112] zone axis. The dark field images show that there is an orientation change as the transmitted beam is shifted from a (220) to a ($\bar{2}$20) reflection spot (Figures 46-47). There is even a shift in the image within the boundary when varying from bright field to dark field (Figures 48-49). The orientation change from shifting the transmitted beam would suggest that the boundary is a twin or a grain boundary. However, the orientation shift from a (220) to a ($\bar{2}$20) spot is an exremely low angle of tilt for a high

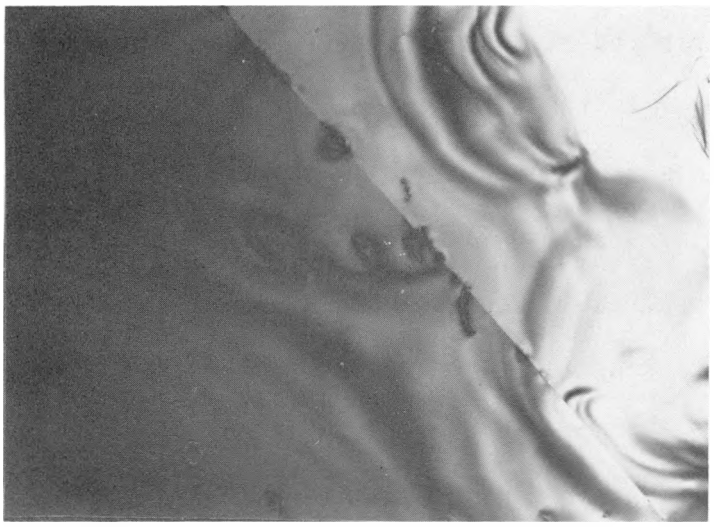

Figure 38a. Coherent twin boundary with both sides oriented at [011] zone axes but at 70° angles to each other. Note that dislocations are pinned to it (10,000X).

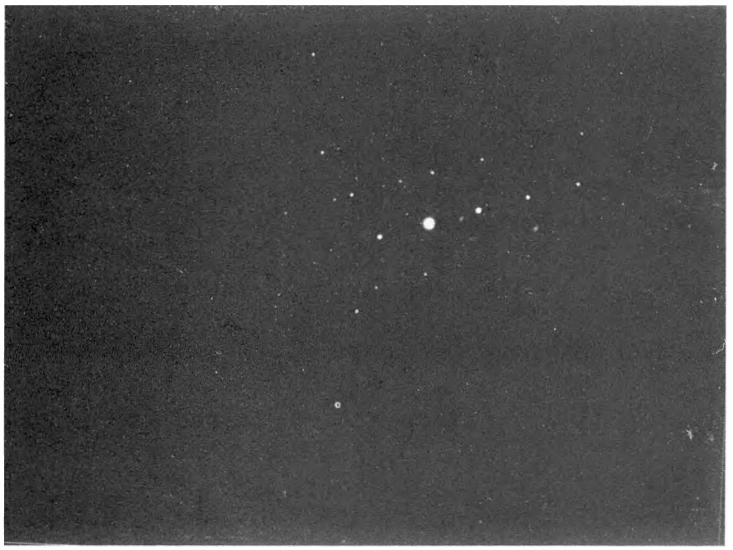

Figure 38b. Diffraction pattern of above twin boundary.

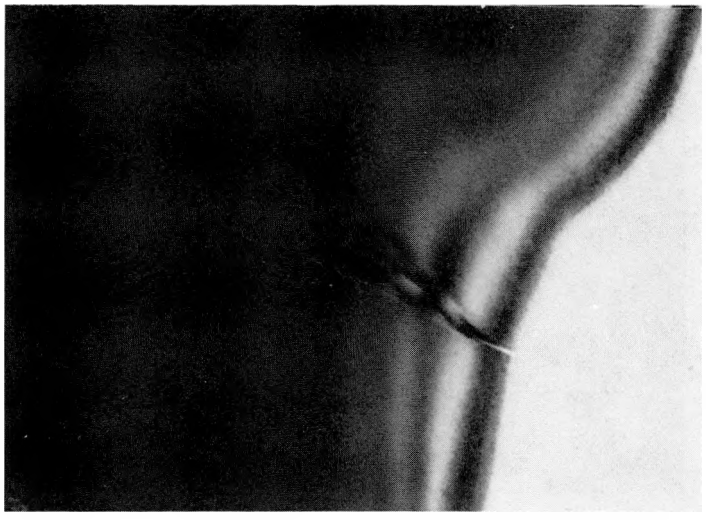

Figure 39. A single stacking fault oriented at a zone axis of [111] (100,000X).

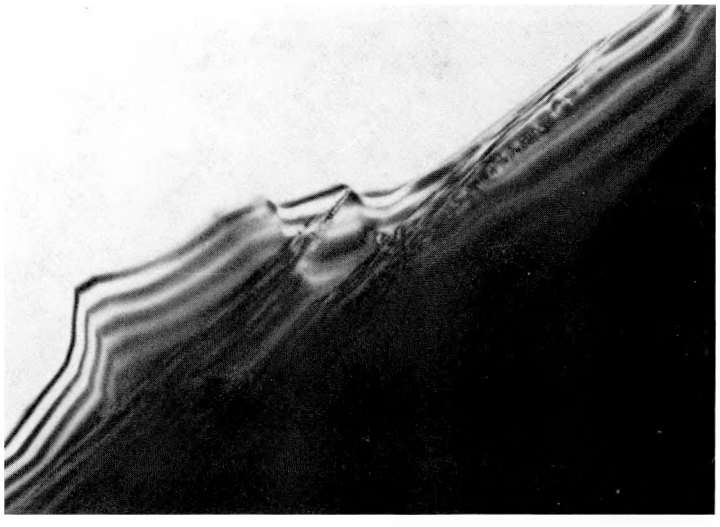

Figure 40. A typical group of stacking faults oriented at a [001] zone axis (20,000 X).

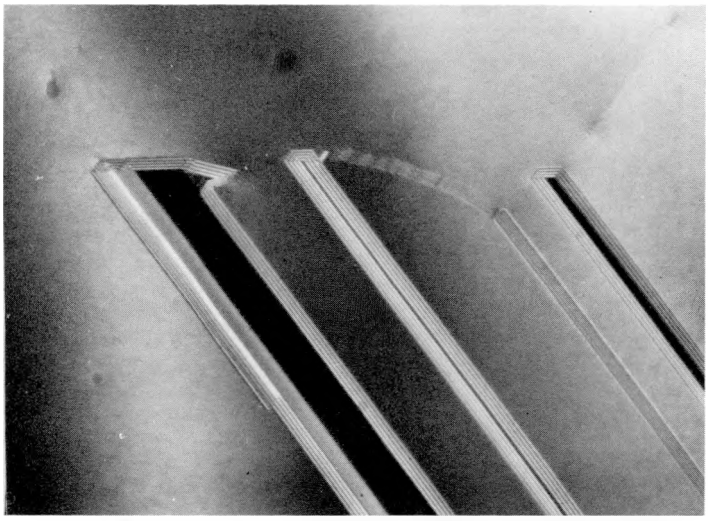

Figure 41a. Dark field photograph of one end of a group of stacking faults contained within the sample. This group is oriented at a zone axis of [011] (30,000X).

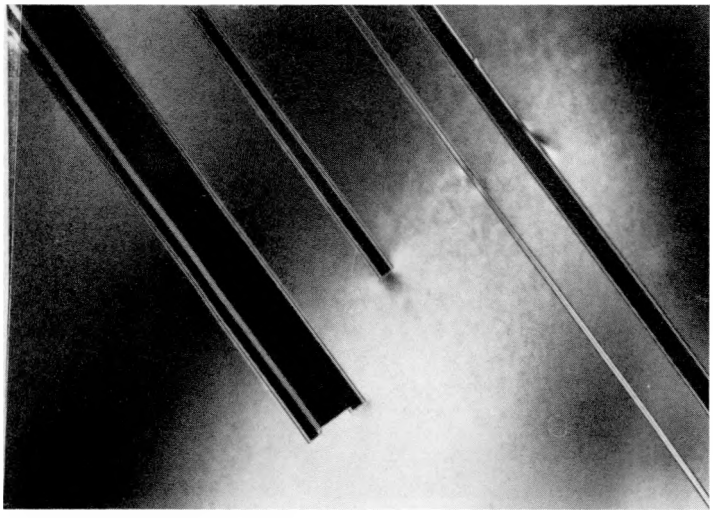

Figure 41b. Dark field photograph of the other end of the above stacking faults (30,000X).

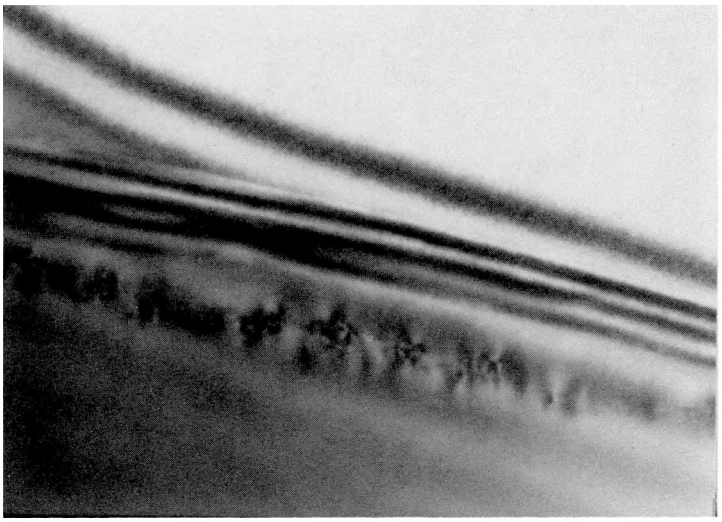

Figure 42. A typical line of dislocation tangles near a boundary in an LASS sample (100,000X).

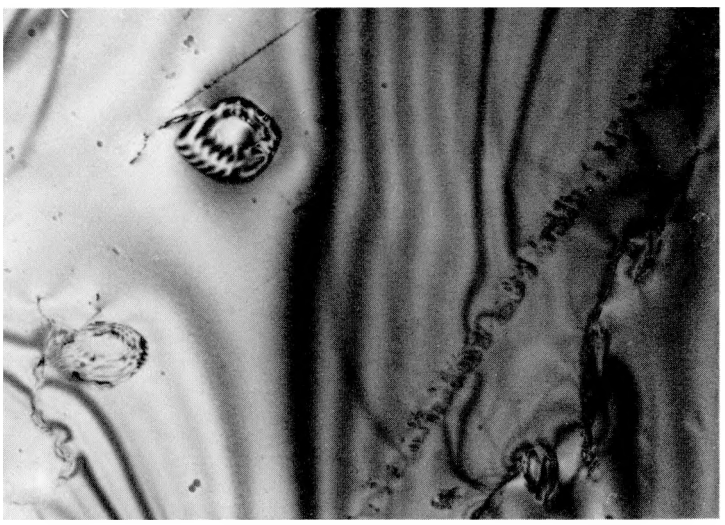

Figure 43. Lines of precipitates with dislocation tangles and some single precipitates with dislocation tangles around them (10,000X).

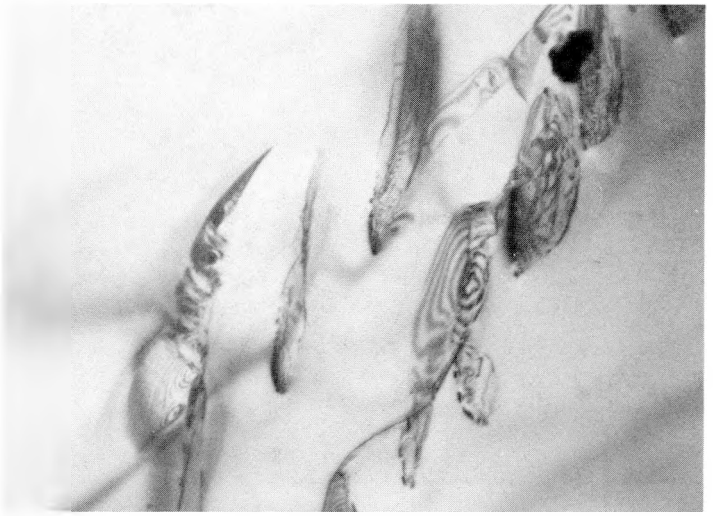

Figure 44. A line of precipitates with dislocation tangles around them (10,000X).

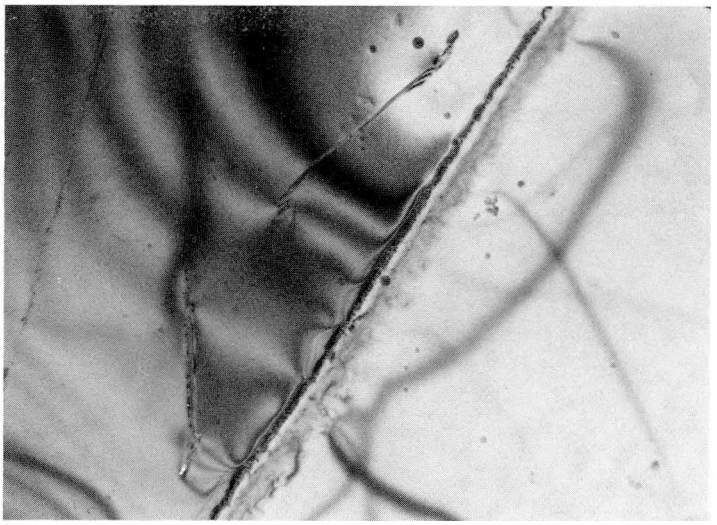

Figure 45. A typical planar boundary oriented near the [112] zone axis (10,000X).

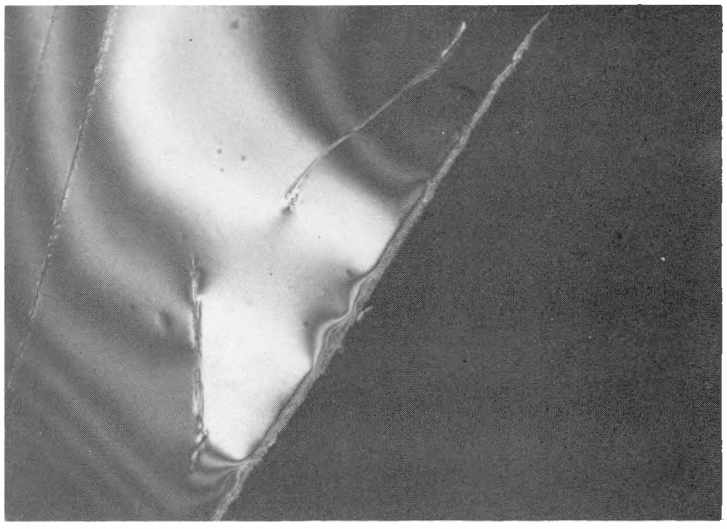

Figure 46. Dark field image of Figure 45 oriented on a (220) spot of a [112] zone axis (10,000X).

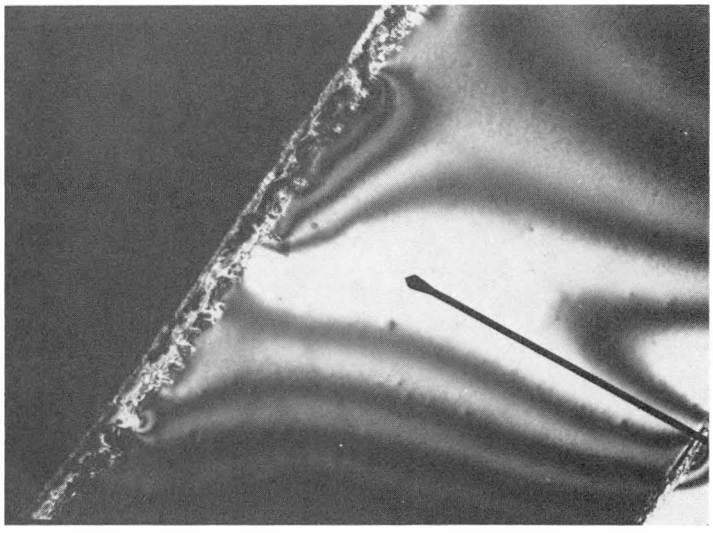

Figure 47. Dark field image of above boundary but oriented on the ($\bar{2}20$) spot of a [112] zone axis (10,000X).

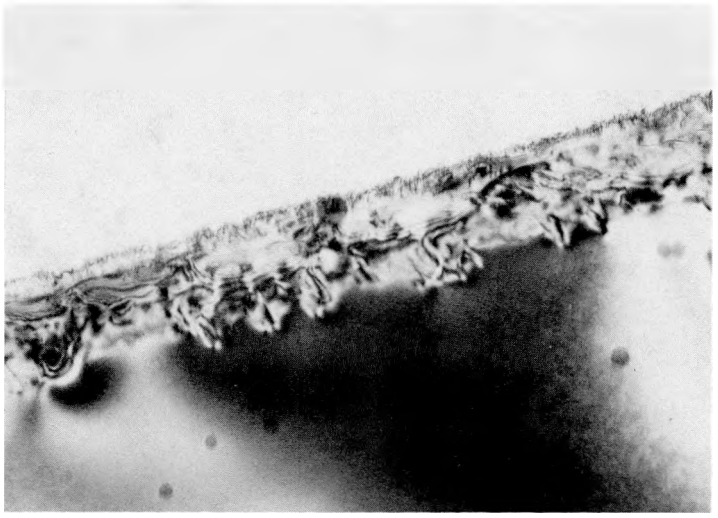

Figure 48. Another area on the planar boundary seen in Figure 45 but oriented at a [011] zone axis (30,000X).

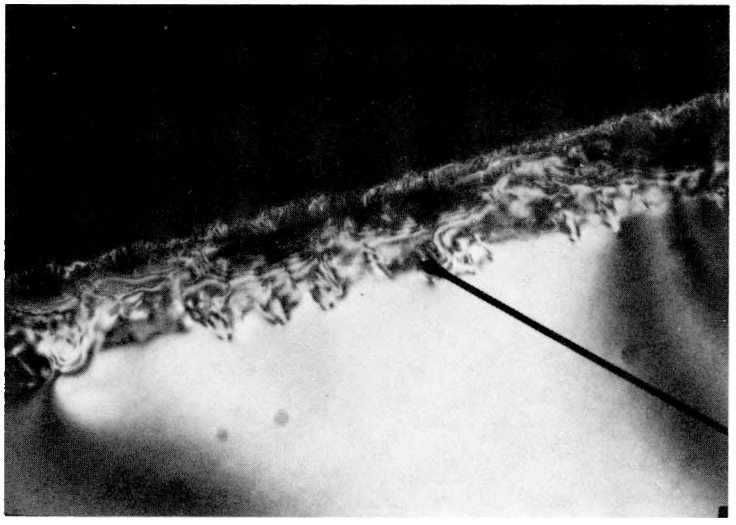

Figure 49. Dark field image of above boundary (30,000X).

angle grain boundary or a twin to be a feasible choice. Thus, it was assumed that these planar boundaries were low angle boundaries with very closely packed lines of tangled dislocations or lines of precipitates with dislocation tangles.

Another different planar feature observed can be seen in Figures 50-52. This feature was oriented at a [100] zone axis. It looks similar but not exactly like a twin or stacking fault with precipitates pinned to it. It was assumed to be a stacking fault with precipitates pinned to it since there was no noticeable change in the features when shifting from a bright field to a dark field image. Although this feature does not look exactly like the other stacking faults observed in this material, it was felt that this was due to the mechanical lapping and chemical cleaning of only this sample in preparation for electron channeling, which may have preferentially etched this feature.

Unfortunately, surface contamination was present on those ESP and LASS samples ion milled from only one side. A sample of pure, single crystal silicon was extensively ion milled from one side only to determine the composition of the contamination typically seen on those samples ion milled from one side only. It was felt that this contamination, seen on both the standard and the experimental samples, was only on the surface because, as the samples were tilted in the TEM, the contamination would rotate with the samples and not remain stationary, as a defect would.

Energy Dispersive Spectrometry (EDS) and Electron Energy Loss Spectroscopy (EELS) were used to analyze the composition of the surface

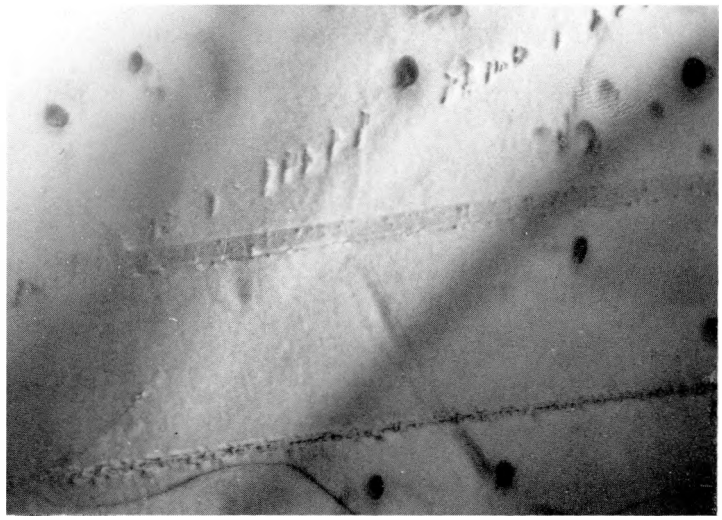

Figure 50. Bright field image of three planar features lined up and oriented at a [100] zone axis (20,000X).

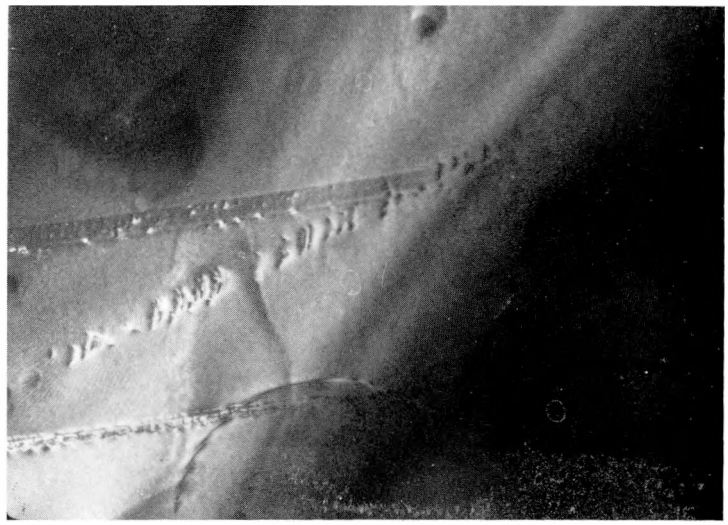

Figure 51. Dark field image of above planar features (20,000X).

Figure 52. Bright field image of one of the three planar features in Figure 51 (50,000X).

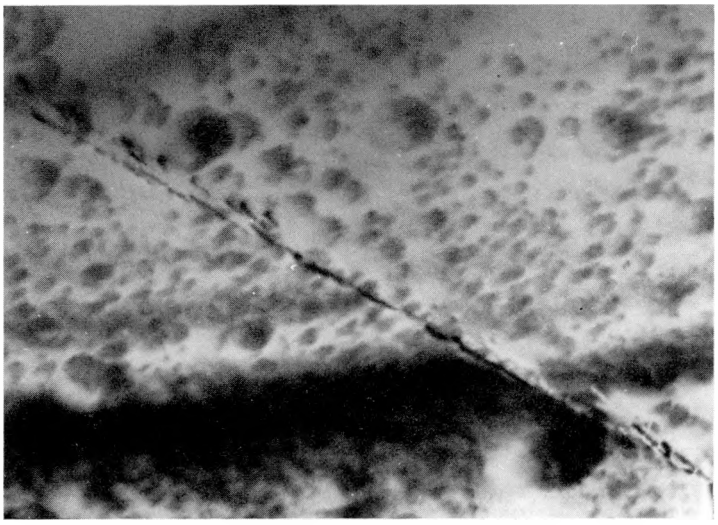

Figure 53. Bright field image of a single crystal silicon sample extensively ion milled from one side only (30,000X).

Figure 54. Another area of the pure silicon sample extensively ion milled from one side only. Note the two parallel lines of dislocation tangles (30,000X).

Figure 55. Another area of the above sample. Note the three lines of dislocation tangles crossing (20,000X).

contamination on both a standard sample and an LASS sample. The EDS results for the matrix of an LASS sample showed the presence of silicon, chromium, iron and copper (See Figure 56). The results for a large particle of contamination on the LASS sample showed the presence of silicon, chromium, iron, copper and a very small amount of argon (see Figure 57). Trace amounts of zinc, argon and potassium may also be present in both the matrix and the large particle, but could not be confirmed due to the small quantity of material analyzed. The EELS results on both the matrix and the large particle of contamination showed the presence of carbon, chromium and/or iron and oxygen and/or chromium (see Figure 58-59). The EDS results on the standard sample of both the matrix and the large particle showed the presence of silicon, argon, chromium, iron, nickel, copper and zinc (see Figures 60-61). Trace amounts of sulfur may also be present, but again could not be confirmed. It was felt that the source of the iron, nickel and chromium were coming from something made of stainless steel and that the source of the copper and zinc were coming from something made of brass. The close similarities in the analysis of both the matrix and the large particle of contamination were due to the relatively small size of the particle in relation to the detection region of both the EELS and the EDS. It was also felt that there was such a small difference between the analysis of the particle and the matrix, because the contamination was spread more finely over the entire surface, rather than concentrated into a few large particles on the surface.

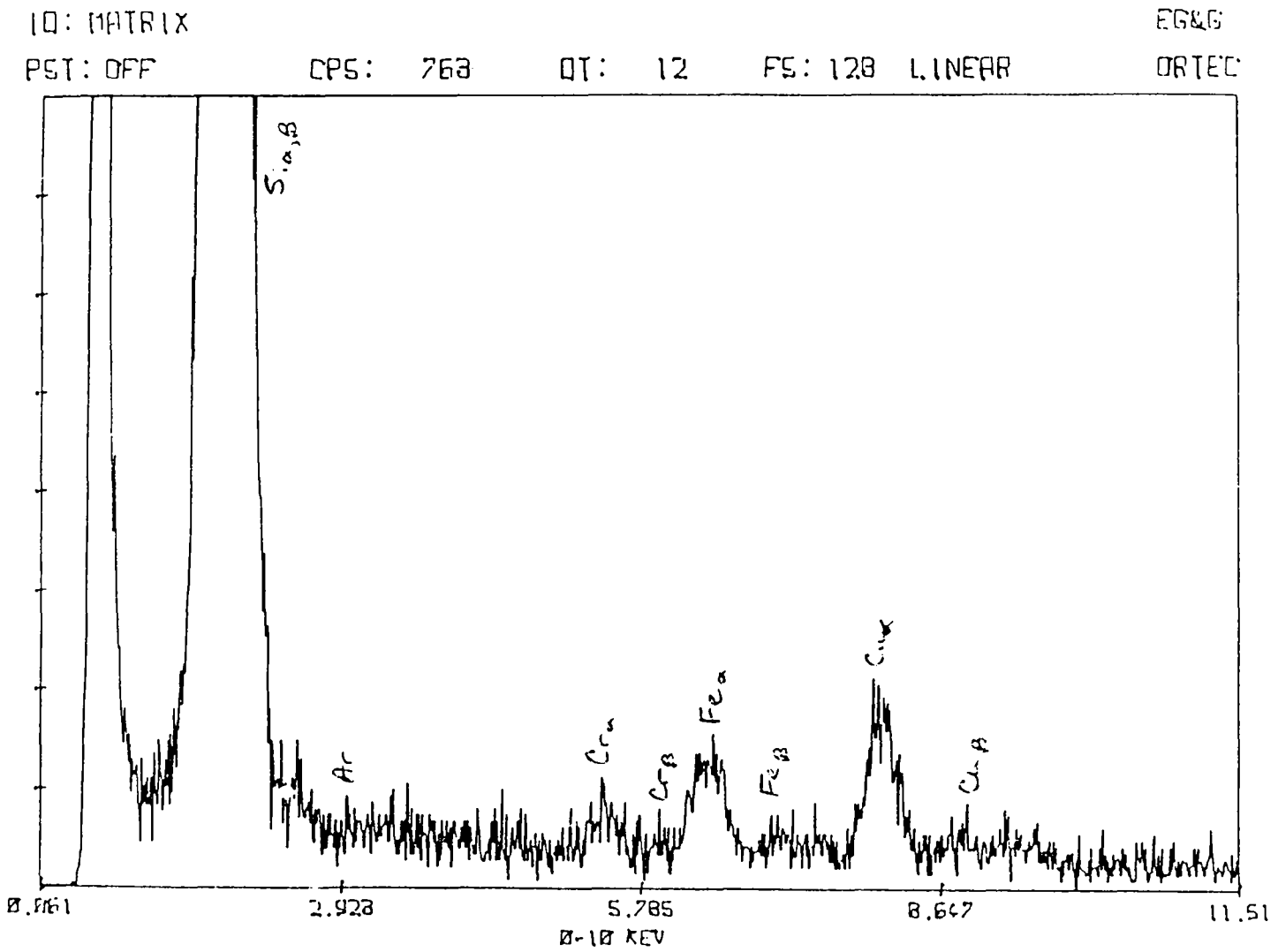

Figure 56. EDS graph from the matrix of an LASS sample.

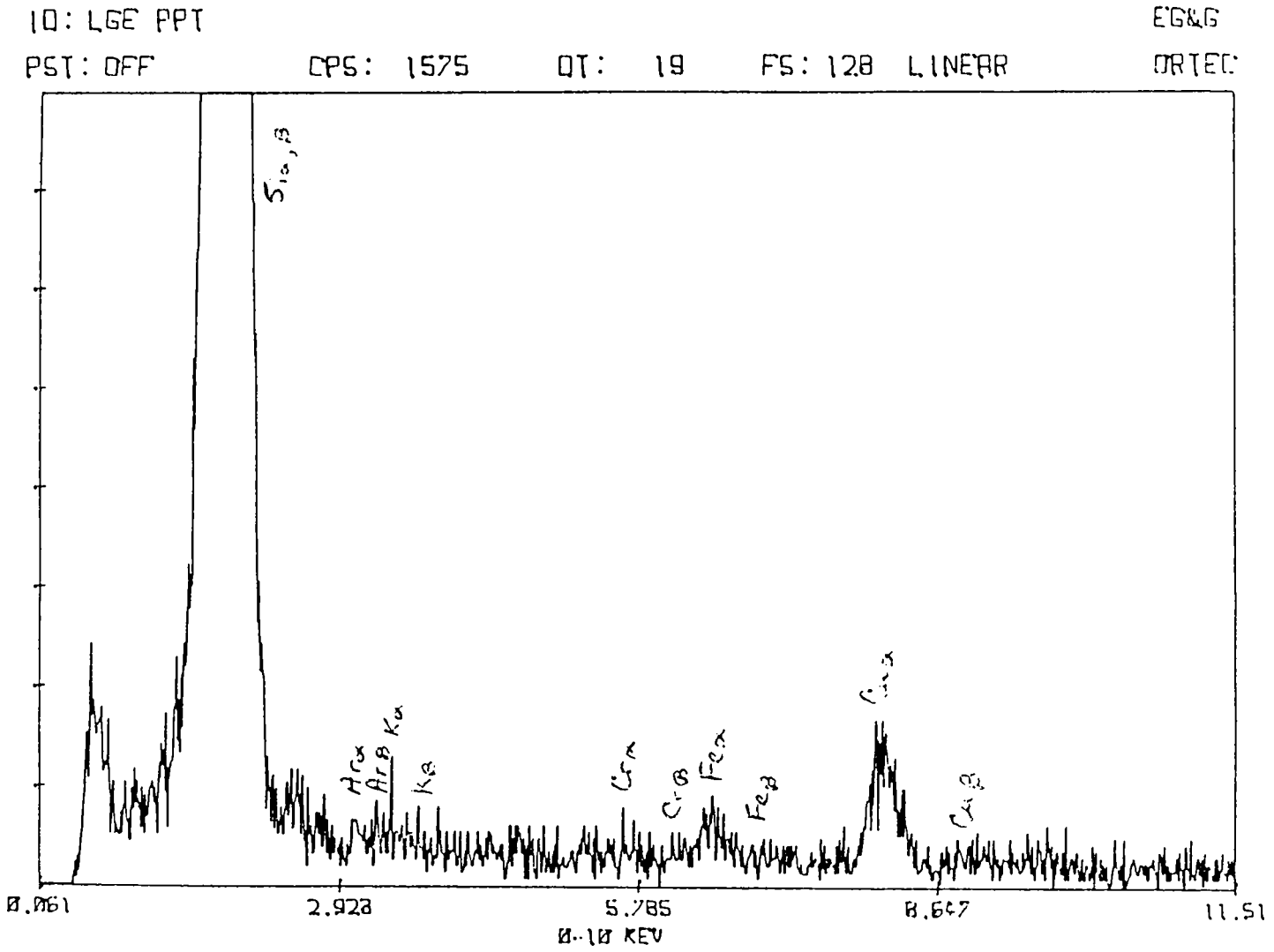

Figure 57. EDS graph from a large particle on an LASS sample.

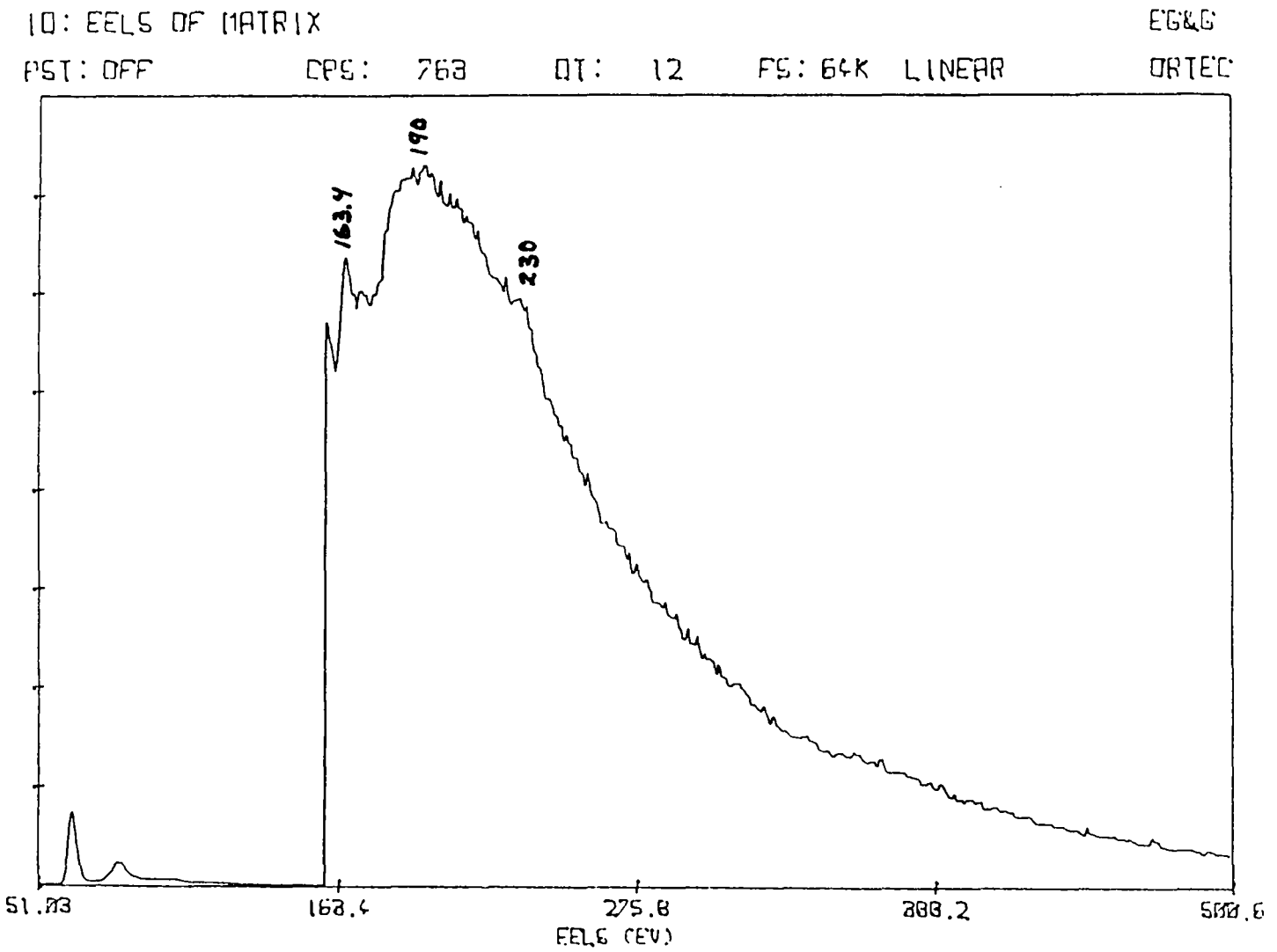

Figure 58. EELS graph from the matrix of an LASS sample.

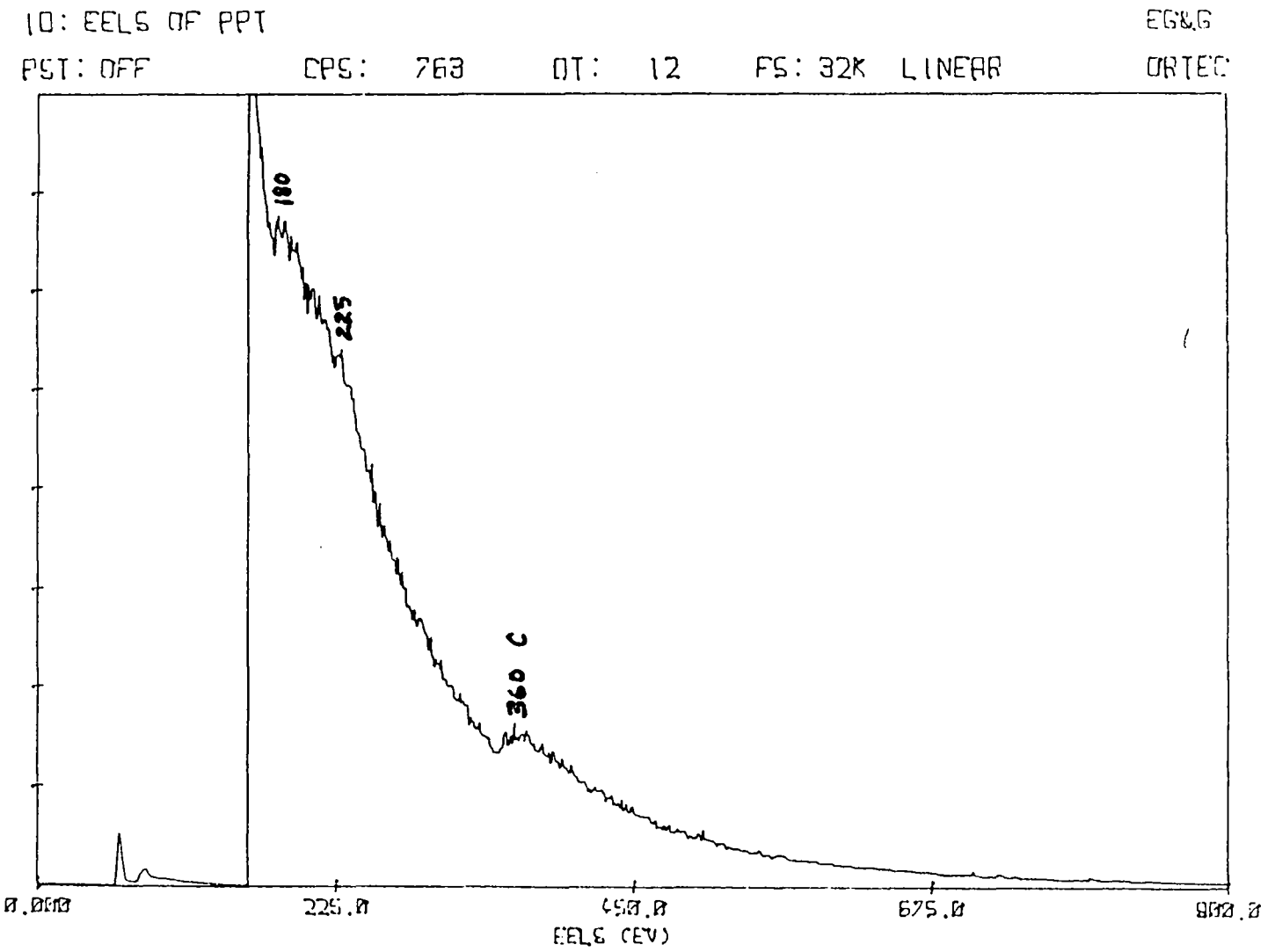

Figure 59. EELS graph from a large particle on an LASS sample.

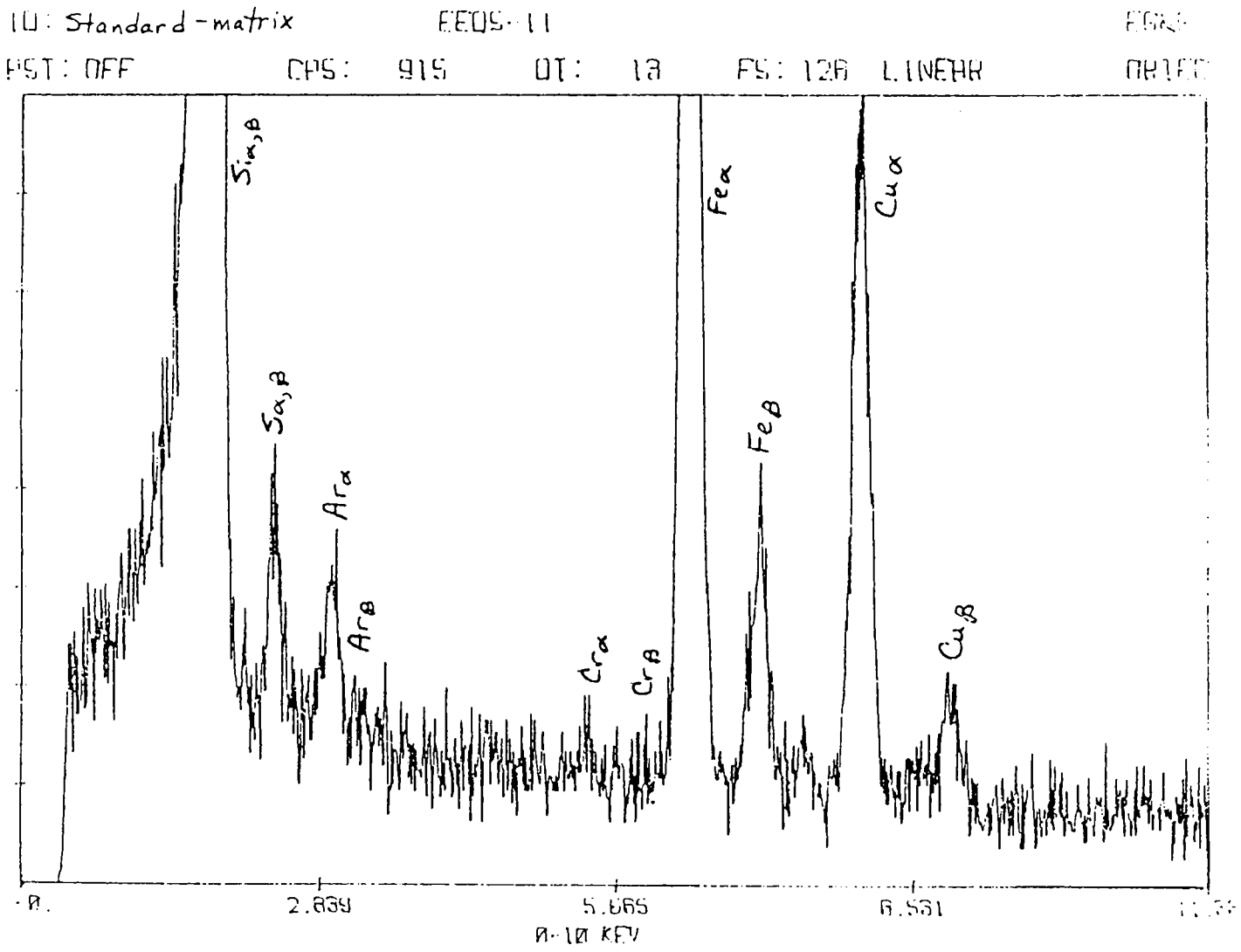

Figure 60. EDS graph from the matrix of an extensively ion milled single crystal silicon sample.

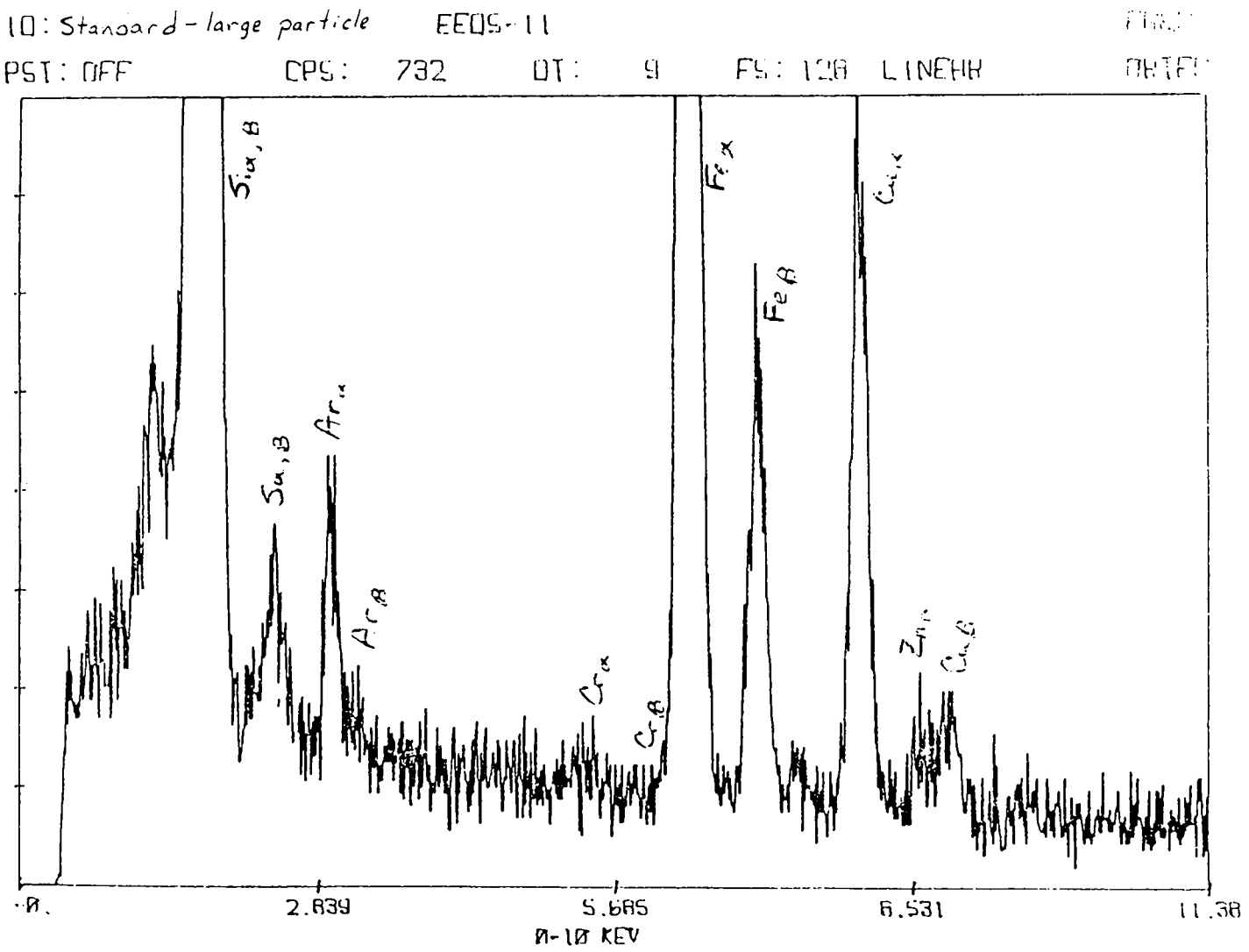

Figure 61. EDS graph from a large particle on an extensively ion milled, single crystal silicon sample.

Energy Materials Corporation (EMC) had mass spectrometry analysis done on some LASS material just after fabrication. This analysis showed the presence of iron, chromium and aluminum [24]. Thus, it was felt that there was contamination from both the fabrication process and from the ion miller. It seemed likely that the almost spherical contamination found on the surface was from the ion miller, whereas the precipitates found embedded in the material were more likely to be from the fabrication process.

Besides surface contamination, the other features seen in the single crystal silicon sample were lines of dislocation tangles observed in Figures 53-55. Obviously, these were formed sometime during the TEM specimen preparation process. However, fewer (approximately half as many) of these lines of dislocation tangles were observed in the standard sample than in the average experimental sample. The standard sample started with fewer fabrication impurities and was ion milled about the same amount of time as the average of the experimental samples. Thus, it was felt that some of the lines of dislocation tangles were induced by the TEM specimen preparation process but that some of the lines of dislocations were characteristic of the sample.

Summary

In summary, the electron channeling studies of the random dendritic LASS sample showed the presence of a few rectangular grains. Surface normals of 81% of the grains were oriented at either [113],

[233], [015] or [2 7 16] and the growth direction was parallel to the {211} family of planes.

The EBIC results of the ESP samples showed long, linear bands of poor EBIC response. The EBIC results of the LASS samples showed the presence of twins, stacking faults, dislocations, grain boundaries and precipitates.

It was observed that for both the ESP and LASS samples that areas of good EBIC response were characterized by relatively few defects whereas areas of poor EBIC response had numerous defects piled together.

CHAPTER 5
DISCUSSION

The electron channeling and EBIC results of the ESP and LASS samples suggests two very different materials. The TEM results show some similarities; however, there are still substantial differences between these two materials.

Electron Channeling

As previously described in the Literature Survey, the LASS material is composed of three types of grain structure: random dendritic, parallel dendritic and twin stabilized planar. Extensive electron channeling studies have not been done on the random dendritic material. However, the results of electron channeling work done by SERI on twin stabilized planar growth material does show some correlation with the random dendritic material studied in this investigation. The electron channeling results showed that the twin stabilized planar growth material was essentially single crystal with a surface normal of <111> [27]. In this study about half of the grains were oriented less than 30° off of the [001] pole and approximately the other half were oriented less than 30° off of the [111] pole. Thus in the LASS material a trend can be seen from the semi-randomly oriented, random dendritic structure (with surface normals oriented partially near the [001] pole and partially near the [111] pole) towards the essentially single crystal, twin stabilized planar structure material (with surface normals oriented at [111]).

In comparison, the electron channeling studies done by SERI on 480 μm thick ESP samples showed long, linear grains several millimeters wide, surface normals of 75% of the area in the center portion were less than 16° off of the [011] direction and the growth direction of about half of the grains were parallel to the (111) plane [20]. Thus there appears to be very little correlation between the electron channeling studies of the LASS and the ESP materials. There is a large difference in grain structure between the two materials, i.e., the long, linear grains of the ESP material versus the almost rectangular grains of varying size of the LASS material. Also, 75% of the ESP surface normals were less than 16° off of the [001] direction whereas 81% of the surface normals of the LASS material were approaching the [111] direction. In comparison, the LASS surface normals showed more randomness in orientation, but less scatter around these orientations. There was only a 5° spread around the appropriate pole as compared to 16° for the ESP samples. However, the four poles, [113], [233], [015] and [2 7 16] were located almost at extremes on the unit triangle map (see the Results section, Figure 13).

Thus, the dominant grain structure of ESP material is similar to the equilibrium crystalline structure achieved by most silicon ribbon growths where "the surface of the ribbon is close to {110}, the growth direction is [211], and significant numbers of twin planes lie parallel to the growth direction" [40]. In contrast, the dominant grain structure of LASS material is more typical of dendritic-web

ribbon growth where the web surface is parallel to the (111) plane, and the web pulling direction is along the <112> direction [45].

These electron channeling results seem reasonable in light of the expected thermal and mechanical influences of the fabrication techniques. The ESP material is pulled vertically and at a slower rate than the LASS material. Thus, the area of the solid-liquid interface is relatively small and the heat of fusion is dissipated at a much slower rate. This dissipation of the heat of fusion is also limited by the rising heat of the melt since the ESP material is vertically pulled. Although this limited dissipation of heat is detrimental for fast growth rates, it is beneficial in maintaining the ribbon above 700°C temperature where extensive dislocation motion can occur by shear [41]. In fcc metals, the most densely packed plane is the (111) plane and thus slip occurs along [110] directions in the {111} family of planes [55]. The maintenance of this ribbon temperature allows dislocation motion and slip to occur along the [110] direction and parallel to the {111} family of planes, which is the dominant grain structure seen in ESP materials. This also correlates with the observations made by Tsuo et al. in which the dominant grain structure was more prevalent in thinner ribbons, where dislocation motion was allowed to occur more easily than in the thicker ribbons [20].

In contrast, the LASS material is pulled horizontally at a very fast rate. The area of the solid-liquid interface is therefore relatively large and the dissipation of the heat of fusion is fairly quick. After nucleation is initiated by the seed crystal, the combination of impurities and the thermal gradients, created by the quick

dissipation of the heat of fusion plus the cooling effects from the cold shoe, promote the growth of dendrites. It has been observed in fcc metals that the [001] direction is the preferred direction for dendritic growth [56]. However, in LASS material the growth direction is parallel to the {211} family of planes. To account for this variance, the stress induced from mechanically pulling at such a fast rate needs to be considered. The random dendritic material is composed of approximately half of the surface normals of the grains oriented near the [001] pole and the other half oriented at the [111] pole. Since the preferred direction for slip in fcc metals occurs along the [011] direction, this would suggest that slip is occurring equally between two operative slip directions. This situation would form a compromise midway between the two operative slip directions which is the [112] pole [57]. This could account for the growth direction proceeding along the [112] direction parallel to the {211} family of planes.

Electron Beam Induced Current

The EBIC results of both the ESP and LASS materials correlates well with previous research done by SERI. The EBIC work done by SERI on ESP materials showed the presence of long, linear boundaries similar in appearance to those observed in our samples [20]. Concerning the EBIC research on LASS materials, general features such as grain boundaries, silicon inclusions, and dislocation clusters similar to those described by SERI [27] were observed in our samples. Short,

straight, non-continuous lines of poor EBIC response were also observed in this investigation and could be stacking faults, as suggested by SERI [27]. These numerous straight lines are much more prevalent in the EBIC montages of the two specimens with surface topography than the one specimen without surface topography. In comparison, the rectangular grain boundaries were only observed in the EBIC montage of the specimen without surface topography. It was noted that it was the specimen without the surface topography that was mechanically lapped and chemically polished for electron channeling. The EBIC montage of this specimen also showed more dislocation clusters than the other two specimens, which were not previously prepared for electron channeling. This could indicate that the dislocation clusters are not prevalent surface features but more characteristic of the interior of the sample and/or that the electron channeling specimen preparation technique may enhance the formation of this defect.

In the LASS samples, the presence of surface topography which is very different from the interior of the sample has been emphasized by the EBIC montages. This formation of substructure can again be attributed to the thermal and mechanical influences of the LASS fabrication technique. Vacancies quenched in during the rapid cooling of the ribbon can be absorbed by the climbing mechanism of dislocations formed during pulling. This movement of "climb whereby edge dislocations change their arrangement from a horizontal to a vertical grouping" [55:364] describes the formation of sub-boundaries. This removal of

vacancies from the lattice and the reduced strain energy of dislocations [55] creates a more favorable strain energy situation for the ribbon.

The effect of grain orientation on the electrical properties was analyzed by comparing the electron channeling and EBIC results. It was observed that there was no direct correlation between the crystallographic and electrical properties. The random dendritic material of this investigation is semi-randomly oriented with no dominant grain structure, so this lack of correlation is not surprising. However, it was thought that for the LASS material, the growth of the dominant grain structure characteristic of the twin stabilized planar material with surface normals near [111], rather than the [011] surface normals characteristic of ESP materials, was electrically beneficial.

Transmission Electron Microscopy

The regions of good electrical, or predominantly light EBIC, responses for both ESP and lass materials were characterized by a low frequency of defects. Those defects which were present were generally defects formed from low strain fields such as stacking faults and dislocations.

The regions of poor electrical, or areas of relatively high concentrations of dark EBIC, responses for both materials were characterized by numerous defects often piled together.

It was thought that the long, linear bands of poor EBIC response observed in the ESP material resulted from the pileups of numerous parallel twins and stacking faults rather than specific grain boundaries. It could not be determined from this investigation

whether these twins were electrically active or whether only the stacking faults in the vicinity were electrically active. It was observed that regions of good EBIC response were often surrounded by regions of poor EBIC response, in which stacking faults were present. It was also noticed that in the ESP material, dislocations seemed to be pinned to only stacking faults. Thus, it appeared that the stacking faults tied up electrically detrimental dislocations, and if located in the appropriate places, could improve the overall electrical response of this material.

In the LASS material, the poor EBIC response was along boundaries of rectangular grains, silicon inclusions and dislocation clusters. The presence of high angle grain boundaries in the TEM results correlates well with the EBIC results. The silicon inclusions observed in the EBIC montages may have been droplets of liquid silicon trapped in the melt, as suggested by SERI [27]. However, a mosaic of low angle boundaries with closely packed, tangled dislocations and/or short, stacking faults seems more feasible from this investigation. The dislocation clusters observed in the EBIC montages seemed to result from dislocation networks around precipitates. In the TEM results of this investigation there is a certain ambiguity as to the sequence of the formation of dislocation networks, stacking faults, and precipitates. The pinning phenomenon of dislocations to twins and stacking faults noted in this material, could also account for the presence of these dislocation clusters, predominantly near long, parallel lines of poor EBIC response.

As suggested by the literature [25] and from the observation of dislocation tangles with precipitates, it was thought that dislocation clusters may act as getters for impurities. Although these dislocation clusters were electrically detrimental, the presence of dislocation clusters in a non-crucial area of the ribbon can improve the overall electrical quality of the LASS material. It was noticed that the predominant orientation of these dislocation networks was along the [112] direction. Again, this orientation could be the outcome of stresses from thermal and mechanical influences on the fabrication process, as previously described.

Fabrication Technique Improvements

Throughout this discussion, references to the development of detrimental defects from thermal and mechanical influences on the fabrication techniques have been made. Thus, the ability to control or minimize these detrimental defects from the fabrication process could improve the conversion efficiency of these materials.

One improvement would be to slow down the pulling speed of the ribbon slightly, so as to reduce the mechanical stresses placed on the ribbon. In the LASS process, the twin stabilized planar material is more preferable than the random dendritic. The slower pulling speeds might also increase the amount of twin stabilized planar growth versus the random dendritic growth by reducing sub-structure growth. However, the cost effectiveness of slowing down the ribbon pull speed would be influential.

The addition of afterheaters or an annealing scheme might also improve both the ESP and LASS ribbon quality. This would allow dislocations, stacking faults and twins to be annealed out of the ribbon or into low energy configurations and possibly decrease the number of pileups of twins and stacking faults. Research on EFG ribbons has shown that the use of annealing afterheaters is effective in reducing the residual stresses formed from the quick dissipation of heat at the interface [39]. However, the cost and energy effectiveness of such an addition would be detrimental.

In the LASS process, different orientations of seed crystals have probably already been experimented with; however, further work could prove beneficial. The initial seed orientation is important for minimizing mechanical stresses introduced at the seed-crystal interface.

The stability of the interface is also important for growing quality LASS material. Impurities were observed in the LASS ribbon and research by Rao and Critella on EFG material has shown that impurities such as carbon and transition metals can be preferentially distributed in the melt by controlling the interface shape [39]. Energy Materials Corporation (EMC) has also pointed out the importance of a stable leading edge in determining the nature of the top surface and the effect of the bulk flow of the melt on the interface in influencing the amount of twin stabilized planar versus random dendritic material grown. The incorporation of a baffle wall with a window in the center, positioned between the fifth zone for bulk melting and the other four zones, may reduce melt turbulence near the interface, plus sieve out heavy metal impurities. However, after some

time there will be increased impurities from the dissolution of the baffle wall, but this improvement should still prove cost effective.

CHAPTER 6
CONCLUSIONS

It was concluded from this investigation that the ESP and LASS materials are very different. The dominant grain structure of the ESP material is characterized by long linear grains, surface normals along the [011] direction and growth directions parallel to the (111) plane. The random dendritic grain structure of the LASS material is semi-randomly oriented and approaches the dominant grain structure of the twin stabilized planar growth material. This dominant grain structure is characterized by the presence of a few rectangular grains, surface normals along the [111] direction and growth directions parallel to the {211} family of planes.

It was obsreved that for both the ESP and LASS samples that areas of good EBIC response had relatively few defects piled together. The ESP material was characterized by long linear bands of poor EBIC response in which the pileup of twins, stacking faults and dislocations were observed. The LASS material was characterized by poor electrical response along boundaries of rectangular grains, silicon inclusions and dislocation clusters in which grain boundaries, stacking faults, twins and precipitates surrounded by dislocation networks were observed.

It was felt that the poor electrical response was related to defects formed by the mechanical pulling during sheet formation. As suggested by the literature [25] and from the observation of dislocation tangles with precipitates, it was thought that dislocation clusters may

act as getters for impurities and thus improve the overall electrical response of the material.

CHAPTER 7
FUTURE WORK

The combination of EBIC, to develop a montage of the overall area from which areas of interest could be selected, with STEBIC/STEM for direct correlation of electrical to microstructural properties could be pursued in the future.

The ability to complement the STEBIC/STEM with lattice imaging using HVEM would also be beneficial. As described in the Literature Survey, dotted EBIC contrast observed in EFG, SOC, etc. materials was thought to be due to the minority carrier recombination along coherent second order {111}/{115} twin boundaries [40]. Coherent second order twin boundaries may also be present in ESP and LASS materials. The use of HVEM would enable the direct correlation of electrical effects with coherent first or second order twin boundaries.

Quantifying or at least semi-quantifying the EBIC or STEBIC data could also be pursued further. By quantifying the EBIC data, a more exact definition of an electrically poor or good region could be described.

Weak beam techniques on the TEM could also be employed in the future. The dislocation clusters observed in LASS materials are heavily strained and there is a lot of dislocation contrast associated with this type of defect. The use of the weak beam technique would reduce the amount of dislocation contrast so that it may be possible to determine the exact cause of the clusters.

Ideas suggested in this thesis in the Fabrication Technique Improvements section of the Discussion chapter could also be tested, e.g., evaluating microstructural and electrical effects of varying the pull rates in the LASS process. The effects of an afterheater or an annealing scheme before device fabrication on the electrical and microstructural properties would be interesting. The effects of using a different setup for the scraper or furnace to reduce contamination, i.e., cooling the scraper tip or using different materials, on the electrical and microstructural properties could also be evaluated.

APPENDIX [16:170]
STANDARD WAFER CLEANING AND POLISHING PROCEDURES

Standard Wafer Cleaning Procedure

1. Scrub with cotton swab soaked with trichloroethylene (TCE).
2. Boil in TCE for 5 minutes.
3. Boil in fresh TCE for 5 minutes.
4. Boil in acetone for 5 minutes.
5. Boil in methanol for 5 minutes.
6. Rinse in deionized water ($\rho \gtrsim 10$ MΩ-cm) for 5 minutes.
7. Dip in 1 H_2SO_4:1 H_2O_2 solution, v/v, for 10 minutes.
8. Remove oxide by dipping in 1 HF:9 H_2O solution, v/v, for 10 seconds.
9. Rinse in deionized water for 5 minutes.
10. Blow dry with N_2 gas gun.

Standard Wafer Polishing Procedure

1. Clean and degrease by following steps 1-6 above.
2. Swirl wafers in a solution of 2 HF:15 HNO_3:5 Ch_3COOH, v/v for 10 minutes.
3. Rinse in deionized water for 5 minutes.
4. Blow dry with N_2 gas gun.

REFERENCES

1. M. Sittig, Solar Cells for Photovoltaic Generation of Electricity—Materials, Devices and Applications, Noyes Data Corp., Park Ridge, NJ (1979).

2. K. Kimura, S. Koyama and H. Watanabe, Proceedings of the Sixteenth IEEE Photovoltaic Specialists Conference, IEEE, New York, NY, 19 (1982).

3. R. C. Neville, Solar Energy Conversion: The Solar Cell, Elsevier Scientific Publishing Co., Inc., New York, NY (1978).

4. C. A. Sorrell, Rocks and Minerals, Golden Press, New York Western Publishing Co., Inc., Racine, WI (1973).

5. S. K. Ghandi, VLSI Fabrication Principles-Silicon and Gallium Arsenide, John Wiley and Sons, Inc., New York, NY (1983).

6. J. J. Loferski, Journal of Applied Physics, 27, 777 (1956).

7. D. M. Chapin, C. S. Fuller and G. L. Pearson, J. Appl. Phys., 25, 676 (1954).

8. K. L. Chopra and S. R. Das, Thin Film Solar Cells, Plenum Press, New York, NY (1983).

9. J. L. Hurd and T. F. Ciszek, Journal of Crystal Growth, 59, 499 (1982).

10. D. N. Jewett, H. E. Bates and J. W. Locher, Proceedings of the Sixteenth IEEE Photovoltaic Specialists Conference, IEEE, New York, NY, 86 (1982).

11. P. E. Gray and C. L. Searle, Electronic Principles—Physics, Models and Circuits, John Wiley and Sons, Inc., New York, NY (1969).

12. B. Cunningham, H. P. Strunk and D. G. Ast, Grain Boundaries in Semiconductors, edited by H. J. Leamy, G. E. Pike and C. H. Seager, Elsevier Science Publishing Co., Inc., New York, NY, 51 (1982).

13. B. G. Streetman, Solid State Electronic Devices, Prentice-Hall, Inc., Englewood Cliffs, NJ (1980).

14. J. G. Fossum and F. A. Lindholm, IEEE Transactions on Electron Devices, ED-27, 692 (1980).

15. T. W. Jung, F. A. Lindholm and A. Neugroschel, IEEE Transactions on Electron Devices, ED-31, 588 (1984).

16. P. Russell, Ph.D. Dissertation, University of Florida (1982).

17. J. Y. W. Seto, J. Appl. Phys., 46, 5247 (1975).

18. J. H. Rose and R. Gronsky, Appl. Phys. Lett., 41, 993 (1982).

19. M. Watanabe, G. Actor and H. C. Gatos, IEEE Transactions on Electron Devices, ED-24, 1172 (1977).

20. Y. S. Tsuo, J. L. Hurd, R. J. Matson and T. F. Ciszek, IEEE Transactions on Electron Devices, ED-31, 614 (1984).

21. T. F. Ciszek, Proceedings of the Sixteenth IEEE Photovoltaic Specialists Conference, IEEE, New York, NY, 316 (1982).

22. T. Koyanagi, Proceedings of the Twelfth IEEE Photovoltaic Specialists Conference, IEEE, New York, NY, 627 (1976).

23. B. Kudo, Journal of Crystal Growth, 50, 247 (1980).

24. D. N. Jewett and H. E. Bates, Proceedings of the Fourteenth IEEE Photovoltaic Specialists Conference, IEEE, New York, NY 1404 (1980).

25. D. N. Jewett, H. E. Bates and J. W. Locher, Proceedings of the Sixteenth IEEE Photovoltaic Specialists Conference, IEEE, New York, NY 86 (1982).

26. H. E. Bates and D. N. Jewett, Flat Plate Solar Array Project Research Forum on the High-Speed Growth and Characterization of Crystals for Solar Cells, Port St. Lucie, FL, 297 (1983).

27. Y. S. Tsuo, R. J. Matson, J. B. Milstein and T. W. Schuyler, Journal of Crystal Growth, 70, 300 (1984).

28. C. H. Seager and D. S. Ginley, Appl. Phys. Lett., 39, 337 (1981).

29. P. H. Robinson and F. V. D'Aiello, Appl. Phys. Lett., 39, 63 (1981).

30. Y. S. Tsuo, R. W. Hardy and J. B. Milstein, Proceedings of the Sixteenth IEEE Photovoltaic Specialists Conference, IEEE, New York, NY, 1 (1982).

31. J. K. G. Panitz, D. J. Sharp and C. H. Seager, Thin Solid Films, 111, 277 (1984).

32. J. I. Hanoka, C. H. Seager, D. J. Sharp and J. K. G. Panitz, Appl. Phys. Lett., 42, 618 (1983).

33. C. Dube, J. I. Hanoka and D. B. Sandstrom, Appl. Phys. Lett., 44, 425 (1984).

34. Y. S. Tsuo and J. B. Milstein, J. Appl. Phys., 57, 5523 (1985).

35. Y. S. Tsuo and J. B. Milstein, Appl. Phys. Lett., 45, 971 (1984).

36. B. G. Yacobi, R. J. Matson, C. R. Herrington and Y. S. Tsuo, J. Appl. Phys., 56, 557 (1984).

37. Private communication with Dr. A. D. Buonaquisti and S. D. Walck (1984).

38. P. Maycock, Proceedings of the Fourteenth IEEE Photovoltaic Specialists Conference, IEEE, New York, NY, 6 (1980).

39. C. V. Hari N. Rao and M. C. Cretella, Proceedings of the Flat Plate Solar Array Project Research Forum on the High-Speed Growth and Characterization of Crystals for Solar Cells, Port St. Lucie, FL, 547 (1983).

40. B. Cunningham, H. Strunk and D. G. Ast, Appl. Phys. Lett., 40, 237 (1982).

41. D. G. Ast, Proceedings of the Flat Plate Solar Array Project Research Forum on the High-Speed Growth and Characterization of Crystals for Solar Cells, Port St. Lucie, FL,453 (1983).

42. M. H. Leipold, Proceedings of the Flat Plate Solar Array Project Research Forum on the High-Speed Growth and Characterization of Crystals for Solar Cells, Port St. Lucie, FL, 57 (1983).

43. C. S. Duncan, R. G. Seidensticker, J. P. McHugh, R. H. Hopkins, M. E. Skutch, J. M. Driggers and F. E. Hill, Proceedings of the Fourteenth IEEE Photovoltaic Specialists Conference, IEEE, New York, NY, 25 (1980).

44. R. B. Campbell, A. Rohatgi, E. J. Seman, J. R. Davis, P. Rai-Choudhury and B. D. Gallagher, Proceedings of the Fourteenth IEEE Photovoltaic Specialists Conference, IEEE, New York, NY, 332 (1980).

45. G. H. Schwuttke, Flat Plate Solar Array Project Research Forum on the High-Speed Growth and Characterization of Crystals for Solar Cells, Port St. Lucie, FL, 565 (1983).

46. V. Lehmann, H. Foll, L. Bernewitz and J. G. Grabmaier, Flat Plate Solar Array Project Research Forum on the High-Speed Growth and Characterization of Crystals for Solar Cells, Port St. Lucie, FL, 527 (1983).

47. R. G. Rosemeir, Flat Plate Solar Array Project Research Forum on the High-Speed Growth and Characterization of Crystals for Solar Cells, Port St. Lucie, FL, 575 (1983).

48. D. C. Joy, D. E. Newbury and D. L. Davidson, J. Appl. Phys., 53, R81 (1982).

49. K. L. Luke and O. Von Roos, J. Appl. Phys., 55, 2962 (1984).

50. S. M. Davidson and C. A. Dimitriadis, Journal of Microscopy, 118, 275 (1980).

51. P. Hirsch, A. Howie, R. B. Nicholson, D. W. Pashley and M. J. Whelan, Electron Microscopy of Thin Crystals, Butterworth and Co., Ltd., London (1967).

52. M. Von Heimendahl, Electron Microscopy of Materials, Academic Press, New York, NY (1980).

53. J. W. Edington, Monographs in Practical Electron Microscopy in Materials Science, N. V. Phillips Gloeilampenfabrieken, Eindhoven, Holland (1976).

54. D. Fathy, T. G. Sparrow and U. Valdre, Journal of Microscopy, 118, 263 (1980).

55. R. E. Smallman, Modern Physical Metallurgy, Butterworth and Co., Ltd., London (1985).

56. R. M. Brick, A. W. Pense and R. B. Gordon, Structure and Properties of Engineering Materials, McGraw-Hill Book Co., New York, NY (1976).

57. G. E. Dieter, Mechanical Metallurgy, McGraw-Hill Book Co., New York, NY (1976).

Document Control Page	1. SERI Report No. SERI/STR-211-3083	2. NTIS Accession No.	3. Recipient's Accession No.

4. Title and Subtitle
Investigation of Selected Electrically Active Defects in Polycrystalline Silicon Solar Cell Materials, Final Subcontract Report, 30 May 1986

5. Publication Date
March 1987

6.

7. Author(s)
J. Hren

8. Performing Organization Rept. No.

9. Performing Organization Name and Address
Department of Materials Science and Engineering
University of Florida
Gainesville, Florida 32611

10. Project/Task/Work Unit No.
3475.10

11. Contract (C) or Grant (G) No.
(C) ZB-4-02129-2
(G)

12. Sponsoring Organization Name and Address
Solar Energy Research Institute
A Division of Midwest Research Institute
1617 Cole Boulevard
Golden, Colorado 80401-3393

13. Type of Report & Period Covered
Technical Report

14.

15. Supplementary Notes
Technical Monitors: Y. S. Tsuo, J. Benner

16. Abstract (Limit: 200 words) This report presents results of a study on techniques for producing silicon wafers for large-scale, terrestrial, solar energy applications: ESP (edge-supported pulling) silicon sheets and LASS (low angle silicon sheets). Correlations between electrical properties and structural and microstructural properties were investigated. Structural properties were analyzed using selected area electron channeling (SAEC); electrical properties were described by means of electron-beam-induced current (EBIC). The transmission electron microscope (TEM) was used to analyze microstructural properties. It was found that the LASS material was semi-randomly oriented. In general, the growth direction was parallel to the {211} family of planes. EBIC results of the ESP material showed long, linear bands of poor electrical response. EBIC results of the LASS material showed poor electrical response along grain boundaries and near silicon inclusions and dislocation clusters. TEM results showed a predominance of twins and stacking faults in both the ESP and LASS materials. The LASS material also exhibited grain boundaries, dislocation networks, and precipitates. The poor electrical response may be related to the stacking faults, grain boundaries, and dislocation networks presumably formed by the mechanical pulling during sheet formation. However, the dislocation networks often appeared to act as gettering sites to tie up impurities and thereby improve the overall electrical response of the material.

17. Document Analysis
a. Descriptors Photovoltaic cells ; silicon solar cells ; sheets ; LASS growth method ; electron microscopy

b. Identifiers/Open-Ended Terms

c. UC Categories
63

18. Availability Statement
National Technical Information Service
U.S. Department of Commerce
5285 Port Royal Road
Springfield, Virginia 22161

19. No. of Pages
124

20. Price
A06

☆ U.S. GOVERNMENT PRINTING OFFICE: 1987—773-098/60,005 REGION NO. 8